Rates and Products of Oxidation of Ferrous Iron in Trioctahedral Smectites

Robert J. Kupper[1], Nanqing Zhou[2], Clara S. Chan[2,3], Aaron Thompson[4], Jeffrey G. Catalano[1,5*]

1. Department of Earth and Planetary Sciences, Washington University, Saint Louis, MO 63130, USA
2. School of Marine Science and Policy, University of Delaware, Newark, DE 19716, USA
3. Department of Earth Sciences, University of Delaware, Newark, DE 19716, USA
4. Department of Crop and Soil Science, University of Georgia, Athens, GA 30602, USA
5. McDonnell Center for the Space Sciences, Washington University, Saint Louis, MO 63130, USA

*Corresponding author: catalano@wustl.edu

Submitted to *Geochimica et Cosmochimica Acta*
December 2022

ABSTRACT

Iron(II)-bearing trioctahedral smectites (saponites) form during anoxic alteration of basaltic rock. They are predicted to have been widespread on the early Earth and are observed in the oceanic subsurface today. Smectite structures, including the occupancy of sites in the octahedral sheet, affect iron redox behavior but the rates and products of trioctahedral smectite oxidation have been largely unexplored to date. In this study we synthesized two Fe(II)-bearing trioctahedral smectites, one moderate (22 wt. % Fe) and one high (27 wt. % Fe) in iron content. We then examined the rate, extent, and products of their oxidation by dissolved oxygen, nitrite, and hydrogen peroxide. Dissolved oxygen caused partial oxidation of Fe(II) in the smectites with 14 to 43% of Fe(II) unoxidized after 20 to 30 days of exposure. The rate and extent of oxidation correlated with the dissolved oxygen concentration and the Fe(II) content of the clay. The incomplete oxidation in these experiments is consistent with the mixed-valent trioctahedral smectites observed in oxidized natural samples but contrasts with the complete reoxidation by oxygen shown by chemically- or microbially-reduced dioctahedral smectites. Oxidation of structural Fe(II) by 5 mmol L^{-1} nitrite was negligible for the moderate-iron smectite and yielded only ~17% oxidation after 54 days of reaction for the high-iron smectite. Hydrogen peroxide caused rapid and near-complete oxidation of both clays. All oxidized smectites maintained a trioctahedral structure and no crystalline secondary minerals formed based on powder X-ray diffraction and variable temperature Mössbauer spectroscopy. This study demonstrates that trioctahedral smectites exhibit distinct oxidation behaviors from dioctahedral smectites and retain their structure and bulk composition following oxidation. Because trioctahedral ferrous smectites accommodate ferric iron in their structure and are resistant to complete oxidation, transitions from anoxic to oxic conditions likely generate mixed-valence smectites rather than a mixture of new phases. The fate of mixed-valent smectites during diagenesis, and thus the signature of trioctahedral smectite oxidation preserved in the rock record, is unclear. Substantial portions of structural Fe(II) in trioctahedral smectites display slow abiotic oxidation kinetics, indicating that these clay minerals represent potential electron donors for both microaerophilic iron oxidizing and nitrate-reducing, iron-oxidizing microorganisms in altered mafic rocks and related settings.

Keywords: Iron Oxidation; Smectite; Mössbauer Spectroscopy; Redox Kinetics

1. INTRODUCTION

Aqueous alteration of basalts produces Mg- and Fe-rich smectites (Velde and Meunier, 2008). Under anoxic conditions, these minerals incorporate ferrous iron and are predominantly trioctahedral saponite smectites (Alt et al., 1986; Andrews, 1980; Badaut et al., 1985; Kohyama et al., 1973). There are numerous occurrences of Fe(II)-bearing smectites (primarily saponites) in the anoxic subsurface of the oceanic crust as vesicle and fracture infilling and alteration crusts (Alt, 1999; Andrews, 1980; Teagle et al., 1996). Similarly Fe(II) smectites form authigenically in anoxic sediments affected by hydrothermal input in the Atlantis II basin in the Red Sea (Badaut et al., 1985). Analogous terrestrial locations contain Fe(II)-bearing trioctahedral smectites in the Deccan Traps flood basalts (Parthasarathy et al., 2003) and low temperature hydrothermal systems in Iceland (Kristmannsdottir, 1979). Despite its overall composition, the glassy, rhyolitic Oya tuff contains both high-iron trioctahedral and low-iron dioctahedral ferrous smectites (Kohyama et al., 1973) formed from altered mineral fragments. Trioctahedral ferrous smectites are also found intercalated with vermiculite in immature orogenic sediments as a result of alteration of biotite and chlorite (Craw et al., 1995). Subsequent oxidation of these clay minerals in the upper oceanic crust (Alt, 1999; Alt et al., 1986) and in exposed terrestrial environments (Craw et al., 1995; Kohyama et al., 1973) produces Fe(III)-bearing phyllosilicate and oxide minerals.

Trioctahedral smectites likely retained a predominantly ferrous state before the oxygenation of Earth’s atmosphere in the Paleoproterozoic (Lyons et al., 2014) possibly persisting as a dominant marine clay until the deep ocean oxygenated in the Neoproterozoic (Canfield et al., 2007; Shen et al., 2002). The size of this smectite Fe(II) pool on the early Earth can be estimated based on current oceanic crust compositions and alteration depths and extents

(Alt, 1999; Alt et al., 1986). Assuming an area of oceanic crust equal to the modern ocean surface (3.62×10^8 km^2), a depth of crustal alteration of 500 m, a basaltic composition with 9 wt.% FeO_T and Fe(II)/Fe(Total) of 0.84, and 5% total alteration predicts that there was 1.9×10^{19} moles of Fe(II) in smectites and related phyllosilicates in the shallow oceanic crystal of the early Earth. If the ocean prior to the Great Oxidation Event (GOE) contained ~0.1 mmol L^{-1} dissolved Fe(II) (Holland, 2004) then it hosted 1.3×10^{17} moles of Fe(II), assuming as a first approximation a total volume equal to today. These coarse estimates yield a total Fe(II) content of the altered oceanic crust more than 200 times that of dissolved Fe(II) in pre-GOE seawater. Recent geochemical modeling (Hao et al., 2017) and examination of Archean paleosols (Babechuk et al., 2019) suggest that ferrous smectites were present on land and in Archean lacustrine systems in addition to marine settings. Similar clays, possibly as mixed valent phases, also occur in lacustrine mudstones at Gale Crater on Mars (Treiman et al., 2014; Vaniman et al., 2014). Iron-rich smectites may also occur on the surface of Ceres (Ehlmann et al., 2018; Rivkin et al., 2006) and on icy worlds with subsurface oceans (Neveu et al., 2017). Trioctahedral smectites thus represent a large Fe(II) pool on the early Earth that may also occur on potentially habitable bodies in the Solar System.

Despite widespread occurrence in anoxic aquatic environments, trioctahedral ferrous smectites are rarely studied because of the difficulty in obtaining, storing, and purifying samples without causing oxidation (Alt et al., 1986; Andrews et al., 1983; Badaut et al., 1985; Craw et al., 1995). Upon exposure to oxygen, iron in these smectites partially oxidizes (Chemtob et al., 2017; Kohyama et al., 1973) yielding a mixed valent phase similar in composition to well-studied saponite smectite from Griffith Park, California (Treiman et al., 2014). To gain further insight into these clay minerals, studies have investigated synthetic trioctahedral ferrous smectites, characterizing their formation mechanisms (Baldermann et al., 2014), composition, structure, and spectral properties (Chemtob et al., 2015; Fox et al., 2021; Sakuma et al., 2022), as well as oxidation products (Chemtob et al., 2017). Notably, a prior study (Chemtob et al., 2017) found that oxidation of ferrous iron in trioctahedral smectites by dissolved oxygen in air-equilibrated solutions was incomplete after 7 days, although hydrogen peroxide caused rapid and complete oxidation. Hydrothermal recrystallization of these fully-oxidized clays generated nanoparticulate hematite, but it is unclear whether iron was ejected from the clay structure to produce an iron oxide during oxidation or simply was more easily observed after the hydrothermal treatment because of conversion from ferrihydrite to hematite. The kinetics of iron oxidation in trioctahedral smectites, the extent of oxidation under different oxygen concentration, and their reactivity with other potential oxidants remain unexamined to date.

In contrast, the redox chemistry of iron in nontronite and other dioctahedral smectites containing ferric iron has been studied extensively (Komadel et al., 1995; Pentráková et al., 2013; Stucki, 2011; Zhao et al., 2015), providing insight into potential behavior displayed by Fe(II)-bearing trioctahedral smectites. Reduction of dioctahedral smectites may be accompanied by iron migration through vacancies, forming trioctahedral domains (Drits and Manceau, 2000; Fialips et al., 2002b; Manceau et al., 2000a; Manceau et al., 2000b) analogous to trioctahedral ferrous smectites. However, this also creates excessive negative layer charge and may cause interlayer collapse (Khaled and Stucki, 1991; Shen and Stucki, 1994; Shen et al., 1992), features not displayed by trioctahedral smectites natively containing Fe(II). Oxidation of Fe(II) in reduced dioctahedral smectites is typically complete (Komadel et al., 1995; Shen and Stucki, 1994) and may displays two-stage kinetics (Neumann et al., 2008). As noted above, the oxidation rates of synthetic trioctahedral ferrous smectites have not been studied so it is unclear if the incomplete oxidation previously observed (Chemtob et al., 2017) is a result of slow kinetics or a recalcitrant Fe(II) fraction not seen in reduced dioctahedral smectites. Two stage (re)oxidation kinetics for dioctahedral clays is attributed to redox interconversion between two distinct iron sites, possibly related to structural rearrangement in the octahedral sheet following oxidation (Neumann et al., 2008). While reoxidized dioctahedral smectites retain some trioctahedral clusters (Fialips et al., 2002a), the low vacancy content of trioctahedral sheets may preclude the structural changes associated with oxidation of dioctahedral smectites and thus yield distinct kinetic behavior.

Additional aspects of Fe(II) oxidation in smectites remain unresolved despite the extensive investigations of reduced dioctahedral clays. While studies have examined the reoxidation of several dioctahedral smectites in oxygen-equilibrated fluids (Fialips et al., 2002a; Komadel et al., 1990; Komadel et al., 1999), oxidation rates have not been examined under microoxic levels favored by microaerophilic iron oxidizers. Separately, the potential role of nitrite as an oxidant of Fe(II) in smectites is uncertain. This species forms as a reactive intermediary by denitrifying bacteria (Betlach and Tiedje, 1981; Glass and Silverstein, 1998) implicated in oxidation of dissolved Fe(II) induced by these organisms (Klueglein and Kappler, 2013; Klueglein et al., 2014). Prior literature is contradictory regarding whether nitrite abiotically oxidizes structural Fe(II) in reduced dioctahedral smectites, with reports of both negligible reactivity (Zhao et al., 2013) and substantial reactivity (Grabb et al., 2017) on timescales of ten to twenty days.

In this study, two trioctahedral ferrous smectites of different compositions were synthesized and their oxidation rates were determined in the presence of dissolved oxygen at atmospheric (21% O_2) and microoxic (2% O_2) levels. The observed rates were fitted to a kinetic model and then compared across different smectite compositions and oxygen concentrations to explore how oxidation rates and extents vary with these parameters. The rates of oxidation of trioctahedral ferrous smectites with nitrite were also investigated. The products of each experiment were characterized by powder X-ray diffraction (XRD) to evaluate changes to the smectite unit cell and identify possible crystalline secondary phases. Mössbauer spectroscopy was utilized to analyze changes in iron speciation and detect potential secondary short-range-ordered (amorphous or nanocrystalline) iron phases. Products of trioctahedral ferrous smectites exposed to hydrogen peroxide were also studied to assess structural alteration and the possible ejection of iron following near-complete oxidation of structural iron. Through these analyses, we constrain the oxidation behavior of trioctahedral ferrous smectites under exposure to oxidants relevant to both early Earth and modern subsurface environments.

2 MATERIALS AND METHODS

2.1. Synthesis of Trioctahedral Smectites

Two smectites were synthesized using a previously-published hydrothermal sol-gel method (Decarreau and Bonnin, 1986) modified to inhibit iron oxidation during heating (Chemtob et al., 2015). All synthesis steps that did not involve sealed vessels were carried out in an anaerobic chamber (Coy Laboratory Products, 96% N_2, 4% H_2, $O_2 < 20$ ppm). A secondary oxygen trap containing 40% potassium hydroxide and 10% pyrogallol was also employed in the anaerobic chamber. Water used in each step was ultrapure (>18.2 MΩ cm) and deoxygenated through sparging, first with nitrogen gas on the benchtop and then using the gas mix inside the anaerobic chamber. Dissolved oxygen concentrations were measured colorimetrically after sparging (CHEMetrics test kit K-7540); all sparged waters contained undetectable dissolved oxygen (detection limit of 2.5 µg L^{-1} , ~80 nmol L^{-1}). Synthesis began with formation of a gel by combining a solution of sodium silicate with a mixture of aluminum, magnesium and iron(II) chloride solutions at a ratio corresponding to a target final smectite composition (**Table 1**). After aging for 24 hours, the gel and fluid were separated by centrifugation, then resuspended in deoxygenated ultrapure water and centrifuged once more to remove any excess salt. The washed gel was resuspended in water once more and adjusted to pH 9 with 0.5 mol L^{-1} sodium hydroxide or 1.0 mol L^{-1} hydrochloric acid. This gel was evenly divided into 200 mL PTFE-lined, steel-jacketed hydrothermal vessels (Parr Instrument Company model 4748A) which were sealed and transferred to a vacuum oven. The oven was backflushed with ultrahigh purity nitrogen gas five times and the gels were then heated at 200°C for 15 days.

Following the hydrothermal treatment, the reactors were transferred back to the anaerobic chamber and synthetic smectites were suspended in a 0.5 mol L^{-1} calcium chloride solution to saturate the interlayer with calcium. After Ca-saturation the smectites suspensions were centrifuged in sealed tubes (Beckman Coulter Avanti 30 centrifuge, F0850 rotor, 16500 rpm) with the fluid then decanted. Excess dissolved salts in the remaining liquid were removed by twice suspending the smectites were ultrapure water and then centrifuging again in sealed tubes, with the supernatant decanted. The wet clay pastes were transferred to a vacuum desiccator loaded with a 4 Å molecular sieve for drying under vacuum. All steps in the washing and drying process were carried out in the anaerobic chamber except for centrifugation. Once sufficiently dry, the samples were ground to a powder using an agate mortar and pestle and sealed in secondary containment within the anaerobic chamber to protect them from inadvertent oxidation.

2.2. Compositional Analysis of Synthetic Smectites

To determine the structural formula for each smectite, a lithium metaborate fusion (Amonette, 1994) method was used. 50 mg smectite was finely ground in an agate mortar and pestle and combined with 350 mg of lithium metaborate flux in a graphite crucible. The mixture was then melted at 1050°C in a muffle furnace for fifteen minutes to produce a glass pellet which was quenched into 40 ml of 10% v./v. trace metal grade nitric acid in a centrifuge tube. This tube was then sealed and placed into a sonicating bath for 12 hours to ensure complete dissolution of the sample. The dissolved sample was diluted and measured on a Thermo Scientific iCap 7400 Duo inductively coupled plasma optical emission spectrometer (ICP-OES). The iron oxidation extent of the solids was determined colorimetrically using a modified 1,10-phenanthroline assay (Tarafder and Thakur, 2013). In place of the leaching procedure Tarafder and Thakur demonstrated for syenite and gabbro, recovered solids were completely dissolved by placing the sample into 10 ml of 20 g/l ammonium bifluoride solution. To ensure dissolution, samples were mixed continuously for 30 minutes in an end-over-end rotator. Following dissolution, 200 ul of the dissolved clay solution was added to two 2 ml cuvettes, one with 1200 ul of water and 200 ul of 5% hydroxylamine hydrochloride to reduce the ferric iron, and another with 1400 ul of water. 200 ul of 10% sodium citrate was then added to each sample to buffer the pH and finally 200 ul of 0.1% 1,10-phenanthroline was added to develop color in the presence of ferrous iron. These cuvettes were then measured in a UV-Vis spectrometer to capture the absorbance at 510 nm. The elemental abundances obtained by ICP-OES were normalized to 22 anionic charges per half unit cell and cations were assigned to either tetrahedral, octahedral or interlayer sites according to their affinity with that site (Amonette, 1994). Iron was divided into ferrous and ferric pools based on the ratio obtained by colorimetry

2.3. Oxidation Kinetics Studies

Each kinetic study was conducted in an artificial freshwater media (Emerson and Merrill Floyd, 2005) for microaerophilic lithophiles that was chosen to replicate the conditions utilized in microbial cultures, e.g., (Zhou et al., 2022), and consistent with natural bicarbonate-buffered aquatic environments. The media contained 1 mL per liter each of ATCC Vitamin Supplement (ATCC MD-VS) and ATCC Trace Mineral Supplement (ATCC MD-TMS). Full media composition appears in **Table S1**; note that the 0.35 µmol L^{-1} Fe(II) in the media is <0.1% of the total Fe(II) in each experiment. A 10 mmol L^{-1} MES buffer was added to decrease the pH drift over the course of the experiment. For each replicate, 200 mg of smectite was suspended in 100 ml of the media and adjusted to an initial pH of 6.2±0.1 using 1 mol L^{-1} hydrochloric acid. Suspensions were kept in foil-wrapped 125 ml borosilicate serum bottles sealed with butyl rubber septa. Each experiment was conducted in triplicate.

In order to determine the rate of oxidation by dissolved oxygen, either air or a gas mixture of 78% N_2, 20% CO_2, and 2% O_2 was first humidified and then passed through a 0.22 µm filter membrane to each serum bottle at a rate of 50 mL min^{-1}. The gas mixture composition was selected to mirror the headspace used in microaerophilic microbial oxidation studies (Zhou et al., 2022). Suspensions were continuously stirred for the duration of the experiment. Temperature and dissolved oxygen were measured every 10 minutes for the duration of the experiments using a Pyro Science Firesting-O2 optode system with contactless sensor spots mounted on the inside walls of the serum bottles for oxygen, and a temperature probe in a separate smectite-free serum bottle.

Sodium nitrite was added to a second set of 125 mL serum bottles for both smectite compositions filled with 100 ml of media to a concentration of 5 mmol L^{-1}. Nitrite is a reactive intermediary produced during bacterial denitrification that has been shown to accumulate extracellularly (Betlach and Tiedje, 1981) up to mmol L^{-1} concentrations (Kappler et al., 2005; Weber et al., 2006). For both smectite compositions an oxidant-free control was also prepared. These serum bottles were then sealed inside the anaerobic chamber with butyl rubber stoppers. The control and nitrite experiments were kept on a horizontal orbital shaker table at 150 rpm and sampled inside the anaerobic chamber. Nitrite content was monitored using the Griess assay (Ivanov, 2004) on supernatant fluids collected at each time point. An analytical problem prevented nitrite quantification for the experiment with the high-iron smectite.

At each timepoint, a 3 mL subsample of the suspension was collected from each suspension and filtered onto a 0.22 μm PTFE filter membrane inside the anaerobic chamber. The filter was washed with deoxygenated ultrapure water to remove any adsorbed oxidants. Digestion in ammonium bifluoride solution followed by colorimetry was used to measure the extent of oxidation in the smectite sample collected via filtration at each timepoint; this method was identical to that used for the initial compositional analysis. At the end of each kinetic experiment, the remaining smectite suspension in each reactor was centrifuged in sealed tubes and then decanted to remove the reaction solution. The solids were resuspended once in ultrapure water followed again by centrifugation and decanting of the supernatant. The solids were then dried in a vacuum desiccator in the anaerobic chamber and then sealed in secondary containers until used for solid-phase analyses.

The rates of iron oxidation in the oxygen exposed smectites were quantified using a two-term second-order kinetic model whose rates are defined by Equation 1:

$$\frac{d[Fe(II)]}{dt} = k_1 {a_1}^2 + k_2 {a_2}^2 \qquad \text{(Eq. 1)}$$

Where k_1 and k_2 are the two different rate constants that govern the portions of Fe(II) a_1 and a_2, respectively. The integrated form, with the additional non-reactive portion is given in Equation 2:

$$Fe(II)_t = \frac{a_1}{k_1 t(a_1+1)} + \frac{a_2}{k_2 t(a_2+1)} + a_3 \qquad \text{(Eq. 2)}$$

$Fe(II)_t$ is the fraction of iron remaining as Fe(II) at time t and a_3 is the portion of Fe(II) that is recalcitrant to oxidation. This integrated equation was fit to the data with parameters of the model determined in MATLAB using a Levenberg-Marquardt nonlinear least squares regression. Each datapoint was weighted by the experimental uncertainty in that point. The same model was applied to all datasets to enable the comparison of parameters between the studies. A two-term second-order model was chosen in line with previous published analysis of Fe(II) oxidation in smectites (Neumann et al., 2008). This prior work allowed for the interconversion of less reactive (k_1) to more reactive (k_2) sites, with a conversion rate determined through an oxidant spike experiment. The work presented here maintained a continuous flow of oxygen and did not determine an interconversion rate.

2.4. Oxidation by Hydrogen Peroxide

Both synthetic smectites were exposed to hydrogen peroxide in order to produce fully oxidized products. These experiments were not conducted in triplicate because oxidation was predicted to be complete and too rapid to be measured in kinetic studies. A suspension of 20 mg of smectite in 100 ml of media was prepared in a sealed 125 ml serum bottle for both compositions and stirred continuously with a magnetic stir bar. 30% hydrogen peroxide solution was added at a ten to one molar ratio of H_2O_2 to Fe for each suspension, with a needle inserted to vent excess gas buildup. This process was carried out on the benchtop, not in an anaerobic chamber, because hydrogen peroxide decomposes to oxygen. Suspensions were vented and continuously stirred with a stir bar for 24 hours to allow for the decomposition of the remaining hydrogen peroxide before being transferred to the anaerobic chamber. Following oxidation, samples were filtered and stored similarly to other samples. The completion of oxidation was checked using the same colorimetric method to measure iron oxidation as with other samples.

2.5. XRD and Mössbauer Analysis

Powder XRD patterns for the synthesized smectites and reaction products were measured using Cu Kα radiation from an X-ray tube operating at 40 kV with a 40 mA current on a Bruker d8 Advance X-ray diffractometer equipped with a Lynxeye XE energy-dispersive silicon strip detector. Samples were evenly ground using an agate mortar and pestle and measured in a silicon zero-background sample holder. In order to prevent oxidation during measurement an acrylic dome was fitted over the samples to maintain an anaerobic environment. Each sample was measured from 3˚ to 65˚ 2θ with 0.019° steps and 0.8 s integration time per step. By scanning over all 192 strips of the detector for 0.8 seconds each, a total integration time of 153.6 s is achieved for each 2θ position. Positions of the (001) peak and (06,33) *hk* band were determined by least-squares fitting utilizing a pseudo-Voigt profile and assuming a linear background.

Samples from one replicate in each set of experimental conditions were selected for Mössbauer analysis. These were evenly ground using an agate mortar and pestle and then homogenously mixed with boron nitride to achieve 10 mg of iron in each 1 cm round PTFE sample holder. Sample holders were sealed with Kapton tape, and then impulse-sealed in polyethylene pouches to inhibit oxidation during measurement. Spectra were collected at room temperature (295 K) and at both 13 K and 5 K using a liquid helium cryostat. Samples were measured in transmission with a 10 to 50 mCi ^{57}Co-Rh gamma source on a 1024 channel detector. Measurement time was up to 18 h for each temperature, and all measurements were taken between -11 and +11 mm s^{-1}. Fitting of each spectrum was accomplished using the Voigt based fitting module of the Recoil software package (Lagarec and Rancourt, 1997).

3. RESULTS

3.1. Characterization of Initial Synthetic Smectites

The compositions of the two synthetic smectites (**Table 2**) are consistent with trioctahedral saponites enriched in iron (April and Keller, 1992; Badaut et al., 1985; Kohyama et al., 1973; Parthasarathy et al., 2003). Layer charge determined from the structural formulas resided solely in the tetrahedral sheet from aluminum substitution for silicon. Despite hosting some aluminum and the small portion of iron that oxidized during synthesis, the octahedral sheets have slight net positive charges because trivalent ion substitutions are largely offset by small vacancy contents. Both smectites have similar octahedral sheet occupancy close to the ideal trioctahedral case. Consistent with previous syntheses of similar phases (Chemtob et al., 2015; Fox et al., 2021), the compositions of the resulting smectites were depleted in magnesium relative to the ratios of components in the initial precipitating solutions. The initial Fe:Mg:Al ratios for the precipitating fluids (**Table 1**) were 40:40:20 and 60:20:20 for the resulting 53:24:23 and 70:08:23 smectites, respectively. In both cases iron and aluminum appear as a higher proportion of the resulting composition relative to magnesium than in the precipitating fluid.

XRD patterns for both smectites indicate the presence of no other detectable crystalline mineral phases (**Fig. 1**). Asymmetry seen in some features is typical for turbostratically-stacked phyllosilicates (Brown, 1982; Moore and Reynolds, 1997). Positions of the (06,33) *hk* band are consistent with trioctahedral smectites (Moore and Reynolds, 1997), including smectites of similar composition (Chemtob et al., 2015). The (001) peak positions indicate predominantly two layers of water in the Ca-saturated interlayer (Watanabe and Sato, 1988).

Room temperature Mössbauer spectra for the two smectite compositions (**Fig. 2**) were well fit by a single doublet each for Fe(II) and Fe(III) (**Table 3**). The proportion of Fe(III) to Fe(II) in the synthesized clays determined by Mössbauer spectroscopy were in agreement with colorimetric measurements (**Table 4**). Spectra of both compositions begin to magnetically-ordered at lower temperatures, with the onset of ordering observed at 13 K for the high-iron smectite and at 5 K for the moderate-iron smectite (**Fig. 2**). Mössbauer spectra of unoxidized samples at low temperature show a pattern consistent with the nascent emergence of ferrous octets with a magnetic ordering temperature that increases with increasing Fe(II) content (Ballet et al., 1985; Rancourt et al., 1994; Ribeiro et al., 2009; Rothwell, 2019). These low-temperature spectra are similar to those of fully-reduced nontronites or other layer silicates with significant ferrous substitution (Cardile et al., 1986; Rancourt et al., 1994; Stucki, 2011). The partially-ordered ferrous octet at low temperature can be modeled using a Full Static Hamiltonian method, but this there is still debate over the interpretation of the parameters (Rothwell, 2019). For our purposes here, which relate mostly to oxidation extent, we only qualitatively interpret these low temperature spectra and focus quantitative interpretation on the 295 K spectra.

3.2. Rates and Extents of Oxidation of Fe(II) in Smectites

3.2.1. Oxidant-free controls

Negligible oxidation of ferrous iron in the smectites occurred during control studies conducted in the absence of oxidants (**Fig. 3**). Measured Fe(II) / Fe(Total) ratios were slightly lower than those obtained during initial characterization, which we attribute to prolonged exposure to traces of oxygen in the anaerobic chamber used for these studies. An increase in pH of ~0.4 units occurred over the course of the experiments (**Table 4**). This is attributed to CO_2 degassing after decapping the reactors and measuring the pH in the low-CO_2 atmosphere of the anaerobic chamber.

3.2.2. Oxidation by Dissolved Oxygen

Dissolved oxygen incompletely oxidizes both smectite compositions, irrespective of oxygen concentration (**Fig. 3**). Oxidation initially proceeded rapidly for both compositions but then slowed despite ferrous iron remaining in the smectite structures. The rate and extent of oxidation were greater for the high-iron composition clay compared to the moderate-iron composition. Atmospheric O_2 levels produced more rapid and complete oxidation compared to 2% $O_2(g)$ in the microoxic studies, regardless of smectite composition.

Dissolved oxygen levels took several hours to reach equilibrium in both the air-equilibrated and microoxic studies (**Fig. S1**). Pre-equilibration of the solution with O_2 was not possible because the smectites needed to first be suspended and hydrated under anoxic conditions prior to initiating the experiments. Initial gas-water equilibration with O_2 was more rapid in studies using atmospheric oxygen than in the microoxic experiments. This is likely due to high initial rates of consumption by the oxidation of ferrous iron while gas composition and flow rates remained constant. Dissolved oxygen levels after this point remained stable and primarily varied with temperature, which affects oxygen solubility. In each experiment, pH increased by 0.4 to 0.7 units over the course of the experiment (**Table 4**), again likely from CO_2 degassing during pH measurement in the anaerobic chamber. The effect was smaller in the microoxic studies, potentially because of buffering from the greater CO_2 content in the gas mixture.

3.2.3. Oxidation by Nitrite

In contrast to reaction with dissolved oxygen, suspensions of both smectites in media containing 5 mmol L^{-1} sodium nitrite showed minimal oxidation over the experimental period of 650 hours for the moderate iron smectite and 1302 hours for the high iron smectite (**Table 4**, **Fig. 4**). The Fe(III)/Fe(Total) of nitrite-exposed samples were generally indistinguishable from oxidant free controls except at long time intervals with the high-iron smectite, with the Fe(II)/Fe(Total) ratio dropping below 0.8 at 580 hours and proceeding to 0.73±0.04 at 1302 hours. For the moderate-iron smectite, no variation in nitrite concentration was observed over the duration of the experiment (**Fig. S2**). An analytical problem prevented quantification of dissolved nitrite for the high-iron concentration experiment. However, the observed iron oxidation requires reduction of only 1.7% of the nitrite in the experiment, smaller than the typical 4.6% standard deviation of nitrite concentrations in the triplicate reactors for the moderate-iron experiment. This amount of nitrite reduction would thus have not been observable.

3.2.4. Oxidation by Hydrogen Peroxide

Oxidation by hydrogen peroxide resulted in an immediate change in the color of the smectite from blue-green to brown. This reaction was accompanied by the release of a substantial amount of gas, presumably O_2 although this was not measured. The extent of oxidation in the smectite measured colorimetrically and by Mössbauer spectroscopy were in close agreement (**Table 4**), with both showing 3 to 6 % residual Fe(II) remained oxidation by hydrogen peroxide.

3.3. Analysis of Oxidation Kinetics

A two site second-order kinetic model as detailed earlier (**Equations 1, 2**) was fit to each dataset from oxidation by O_2 (**Table 5**). Fast and slow oxidation components as well as a recalcitrant Fe(II) fraction were independently fitted for the high-iron smectite results. However, data at short reaction times (<3 h) was not obtained for the moderate-iron smectite at both O_2 concentrations and this prevented accurate fitting of the rate constant for the fast oxidation component. This parameter was fixed to the value obtained from the high-iron smectite experiments using the same O_2 concentration but this precludes comparison of the rate of the rapid component (k_1) between two clays. The moderate-iron smectite reacted with 2% O_2 showed a lower initial Fe(II) concentration than the same smectite immediately after synthesis or in the other experiments (**Table 4**). Kinetic modeling of the results from this experiment obtained only a small contribution of the fast oxidation component. We hypothesize that inadvertent partial oxidation occurred during the experimental setup.

For the high-iron smectite, the rapid component had a rate constant ~5 times greater at 21% O_2 compared to 2% (**Table 5**). While this may suggest kinetic behavior that is not first-order with respect to oxygen partial pressure, dissolved oxygen concentrations took 1 to 4 h to equilibrate with the gas stream; this period of unbuffered oxygen partial pressure was not accounted for in the model. The fraction of oxidized Fe(II) modeled by the fast component was greatest for the high-iron smectite oxidized by air, with this contribution decreasing under lower oxygen partial pressure and for the moderate-iron smectite. For each smectite, the modeled slow oxidation component of the kinetic behavior accounted for a similar fraction of Fe(II) oxidation under both oxygen levels used (**Table 5**). Kinetic modeling produced a smaller recalcitrant Fe(II) fraction for the high-iron smectite compared to the moderate-iron smectite (**Table 5**), consistent with observed difference total Fe(II) oxidation (**Fig. 3**). For both clays, the modeled recalcitrant fraction was greater for experiments with 2% O_2 than with 21% O_2 (**Table 5**).

The extent of oxidation in the control and nitrite-exposed experiments was equal within error to zero in all treatments except the high-iron smectite. We evaluated this using a single first order kinetic term with a recalcitrant portion (see **Supplementary Material**). For the oxidant-free control experiments, the model-obtained rate constants were effectively zero after considering parameter uncertainty (**Table S2**), confirming that no detectable oxidation occurred over the duration of these control experiments. Reaction of the moderate-iron smectite with nitrite yielded a rate constant that was the same order of magnitude as, but smaller than, its uncertainty, indicating that no statistically-significant oxidation occur on the experimental timescale. Reaction of the high-iron smectite with nitrite was the only system to produce a rate constant that was not within error of zero (**Table S2**, **Fig. S3**). However, accurately quantifying the rate of oxidation of this clay by nitrite would require experiments longer than the 54 d duration explored in this study.

3.4. Characterization of Oxidation Products

3.4.1. Powder X-ray Diffraction

No features from crystalline secondary minerals were observed in the XRD patterns of the oxidized smectites but diffraction features associated with layer stacking and lattice size shifted systematically (**Fig. 5, 6**). The (001) peak positions (**Fig. 5**) of the smectites show a general shift to higher angle with increasing extent of oxidation (**Table 6**), resulting in a decreased in d-spacing (**Fig. 7**). The (001) d-spacing for the initial synthetic smectites appear to be systematically larger than for the reacted smectites, deviating from the trend with increasing iron oxidation extent. This may reflect differences in drying between the initial smectites and the reacted smectites. While both were dried in a vacuum desiccator, the initial smectite samples had substantially larger masses (~5 g) than the reacted samples (<200 mg) and thus may have reached different extents of dehydration during similar desiccation times. In addition, suspension in the media solution during the oxidation experiments would alter the interlayer cation composition (this was not measured) compared to the initially Ca-saturated smectites, which would also impact the (001) d-spacing. All of the smectites used in oxidation experiments experienced the same fluid composition and drying procedures and the observed trend among these reacted samples is thus likely robust. The (06,33) *hk* bands (**Fig. 6**) also shift to higher angle after oxidant exposure (**Table 6**), corresponding with a shift towards smaller *b* unit cell parameters. This is consistent with Fe(II) in the octahedral sheet oxidizing to Fe(III), which has a smaller ionic radius (Shannon, 1976). The high-iron smectite displays a more linear relationship between (06,33) d-spacing and extent of oxidation than the moderate-iron smectite (**Fig. 7**). All changes were greatest after reaction with hydrogen peroxide and smallest after reaction with nitrite, consistent with differences in oxidation extent (**Table 4**).

3.4.2. Mössbauer Spectroscopy

Spectra collected at 295 K (**Fig. 8, 9**) show only paramagnetic ordering and a transition from primarily a Fe(II) doublet to an Fe(III) doublet with increasing extent of oxidation. These spectra were thus modeled with one Fe(II) and one Fe(III) site using the Voigt-based fitting module in Recoil (**Table 3**). The resulting Fe(II) and Fe(III) contents were consistent with the extents of oxidation determined by the colorimetric measurements for the oxygen exposed and control samples (**Table 4**). For the nitrite-exposed, high-iron sample, the Mössbauer-derived Fe(III) content is substantially larger than the values determined from colorimetry (**Table 4**). For this treatment only, we hypothesize that inadvertent oxidation occurred during prolonged sample storage between the experiments, which included immediate colorimetric analysis, and the Mössbauer measurements.

After reaction with oxidants, the 13 K and 5 K Mössbauer spectra (**Fig. 8, 9**) are consistent with layered silicate clays with high iron substitution and spectral features that vary in response to the Fe(III) and Fe(II) content (Ballet et al., 1985; Rancourt et al., 1994; Ribeiro et al., 2009; Rothwell, 2019). This includes the emergence of magnetic coupling and ordering (or partial ordering) at low temperatures (generally <13 K) arising principally from magnetic interactions between Fe atoms in next-nearest neighbor positions, for example Fe-O-Fe. Such superexchange (Ballet et al., 1985) possibly results from the high Fe content. The oxidant-free controls maintained the partially ordered ferrous octet observed in the initial smectites at 5K (**Fig. 8, 9**). This ferrous magnetic ordering persists after exposure to nitrite with the emergence of a partially-collapsed ferric iron sextet at 5 K for the high-iron smectite. For the oxygen-exposed and hydrogen peroxide samples, the spectra contain a larger Fe(III) component and the ferrous-magnetic ordering is lost (**Fig. 8, 9**). In the oxygen-exposed moderate-iron smectite, this ferric component persists as a doublet down to 5K, with some evidence of a collapsed feature in the less reduced (2% and 21% O_2) samples that may indicate Fe clustering (Ballet et al., 1985; Rothwell, 2019) . For the high-iron smectite samples, the Fe(II) and Fe(III) doublets are overlain by a weakly-formed and partially collapsed Fe(III) sextet (**Fig. 9**). The samples exposed to hydrogen peroxide displayed the greatest amount of Fe(III) for both the high- and moderate-iron compositions, comprising >94% of the iron in each sample (**Table 4**) and show a strong doublet component in the 5 K spectra and a similar partially collapsed Fe(III) sextet at 5 K for the high-iron sample.

Many layered silicates have low to moderate Fe substitution levels and do not exhibit any hyperfine field splitting or magnetic ordering in their Mössbauer spectra at 5 K. The spectra of these typical clay minerals contain only ferric or ferrous doublets. Any sextets in Mössbauer spectra of such clay samples (even partially-ordered sextets) suggest the presence of secondary Fe-oxide phases. Exceptions to this assumption occur at both at the extreme low-end of Fe substitution, where some non-parametric relaxation can produce an extremely broad sextet (Murad and Cashion, 2004), or at high levels of substitution where clusters of Fe atoms can interact through superexchange and produce hyperfine field splitting and partial or full magnetic ordering (Murad and Cashion, 2004; Rancourt et al., 1994). The latter case applies to the smectites in the present study.

Distinguishing Fe atoms in iron-rich (or extremely iron-poor) layered silicates from secondary iron (oxyhydr)oxides, both of which can exhibit hyperfine ordering at 5 K, using Mössbauer spectroscopy requires collection of spectra at temperatures intermediate between ambient and 5 K (Chen et al., 2017). For Fe(III) atoms in layered silicates, any hyperfine splitting or magnetic ordering present at 5 K usually disappears at 12 K, whereas short-range-ordered iron oxyhydroxides (e.g., ferrihydrite) typically retain magnetic ordering until temperatures exceed 35 to 77 K (Sun et al., 2018; Whitaker et al., 2021). Even the most highly substituted or nanosized short-range-ordered iron oxyhydroxides will nearly always exhibit at least partial ordering by 12 K (Chen et al., 2018; Noor and Thompson, 2022). Thus, by collecting spectra at both 4 to 5 K and 12 to 13 K, Fe(III) in silicates and Fe(III) in secondary oxides can distinguished.

For the samples studied here, oxidation of the moderate-iron smectites, even with H_2O_2, do not produce hyperfine field splitting of Fe(III) atoms at either 13 K or 5 K (**Fig. 8**). We can reasonably conclude that no secondary iron oxides or short-range-ordered iron(III) oxyhydroxides were produced and the Fe(III) exists in generally similar (or uniformly distributed) sites. For the oxidized high-iron smectites, the hyperfine field for one or two Fe sites are split and near their ordering temperature at 5 K (**Fig. 9**). Progressively more oxidized samples (2% O_2, 21% O_2, and H_2O_2 treatments) have similar features so we can evaluate the H_2O_2 sample where near-complete oxidation has occurred. The 5 K Mössbauer spectrum of the H_2O_2-oxidized sample contains an Fe(III) sextet with a low field strength (hyperfine field: 42.3±0.2 T, chemical shift: 0.47±0.02 mm s^{-1}, quadrupole splitting: -0.04±0.02 mm s^{-1}), a collapsed Fe(III) sextet, and an Fe(III) doublet (chemical shift: 0.47±0.2 mm s^{-1}, quadrupole splitting: 1.00±0.02 mm s^{-1}). This could reflect Fe(III) occupying three different sites with the doublet representing isolated Fe(III) atoms (likely in the octahedral sheet), and the full and collapsed sextets representing Fe with two (Fe-O-^{57}Fe-O-Fe) or one (Fe-O-^{57}Fe) next nearest neighbors. The collapsed sextet could also reflect adsorbed Fe(III), perhaps in interlayer sites after partial dissolution of the clay and ion-exchange into the interlayer before or after oxidation. The lack of any hyperfine splitting at 13 K strongly argues against a distinct short-range-ordered Fe oxyhydroxide. This spectral interpretation is consistent with a prior study of reduced, re-oxidized dioctahedral smectites (Ribeiro et al., 2009), which displayed a better developed Fe(III) sextet at 4 K than observed in the present study without formation of secondary Fe(III) oxyhydroxides.

4. DISCUSSION

4.1. Products of Trioctahedral Smectite Oxidation

4.1.1. Structural Changes

The XRD patterns of the oxidized smectites from our experiments reveal minor changes in the smectite structure (**Fig. 5**). Among the reacted smectite samples, a decrease in d-spacing is observed for increasing extents of oxidation (**Fig. 7**). Lessened expandability in dioctahedral smectites has been previously reported following a decrease in layer charge (Komadel et al., 2005). A similar effect may occur in the present study because iron oxidation should decrease the layer charge.

Oxidation also impacted the in-plane structure of the smectites. The (06,33) *hk* bands (**Fig. 6**) of the oxidized smectites shift towards smaller d-spacings with increased oxidation (**Table 6**). These remained in the trioctahedral domain, greater than 1.52 Å (Moore and Reynolds, 1997), after oxidation. The lattice contraction resulting from the smaller size of the ferric ion compared to the ferrous ion does not alter the fundamentally trioctahedral nature of these smectites. The charge-compensation mechanism of the smectite is uncertain because the amount of iron oxidation after oxidation by oxygen or hydrogen peroxide would result in a substantial positive layer charge. For example, the high-iron smectite after reaction with air would have a layer charge of +1.44 if all Fe(III) remained in the structure. While ejection of Fe(III) after oxidation provides a mechanism to offset this extra charge, no new crystalline phases, such as goethite, appear in the XRD patterns that would be associated with the ejection of iron. Similarly, the 13 K Mössbauer spectra of the oxidized samples (**Fig. 8, 9**) show no evidence of sextets, which would be expected for all but the most disordered short-range-ordered iron phases and even then partial ordering would likely be evident (Noor and Thompson, 2022).

4.1.2. Redox Distribution, Magnetic Ordering, and Secondary Phases

Direct attribution of doublets in Mössbauer spectra to specific octahedral iron sites has been shown to be difficult, often leading to inaccurate ratios of sites (Baron et al., 2017; Dyar et al., 2008; Heller-Kallai and Rozenson, 1981; Rancourt, 1994a, b). The majority of the iron incorporated into the clay structure was initially present as Fe(II), with only 6 to 8 mol. % as Fe(III). The low Fe(III) contents of the synthetic clays makes it unlikely that tetrahedral iron is present in the smectite structure, consistent with the single ferric doublet modeled for each initial sample. Ferrous CS values (**Table 3**) were similar to those previously reported for synthetic trioctahedral ferrous smectites (Chemtob et al., 2015) and quadrupole splitting values were intermediate of the two sites used in the modeling in that work. Ferric parameters (**Table 3**) are similarly within the range of ferric values previously reported for oxidized trioctahedral smectites (Chemtob et al., 2017).

While prior work has examined the cryogenic Mössbauer spectra of Fe(II) in trioctahedral mica, chlorite, and serpentine minerals (Ballet et al., 1985; Rancourt et al., 1994), this study is the first to report low-temperature spectra from Fe(II)-bearing trioctahedral smectites. Previous studies have obtained room temperature Mössbauer spectra of natural (Badaut et al., 1985; Kohyama et al., 1973) and synthetic (Chemtob et al., 2015) ferrous smectites. All show similar parameters to the 295 K measurements reported in the presented work, including for the minor ferric component. Reduced dioctahedral smectites provide an additional comparison, with 4 K Mössbauer spectra of a fully reduced sample of the Garfield nontronite (Ribeiro et al., 2009) displaying magnetic ordering of ferrous iron similar to the unoxidized trioctahedral ferrous smectites measured at 5 K in our study. This similarity is consistent with reduction of iron-rich dioctahedral smectites producing trioctahedral domains in the mineral structure (Drits and Manceau, 2000; Fialips et al., 2002b; Manceau et al., 2000a; Manceau et al., 2000b).

Greater oxidation in samples correlated with a smaller quadrupole splitting of the Fe(II) site across both smectite compositions (**Fig. 10**). This is consistent with the behavior displayed by a natural ferrous smectite as it oxidized (Kohyama et al., 1973), which was interpreted to indicate that the oxidized smectite had less distortion surrounding the iron sites than unoxidized smectite. This interpretation matches the effect on quadrupole splitting observed in the octahedrally-coordinated Fe(II) in micas when compressed to 200 kbar (Huggins, 1976). It also agrees with simulations showing that greater distortion of the octahedral sheet of phyllosilicates results in a greater quadrupole splitting for Fe(II) in the structure (Evans et al., 2005). The observed trend in quadrupole splitting (**Fig. 10**) thus suggests that the remaining Fe(II) in more oxidized smectites exists within a less distorted local environment. This could result from the structural shifts following oxidation, i.e., in-plane lattice contraction, but may also indicate that two Fe(II) sites were present in the structures and the more distorted site preferentially oxidizes. The quadrupole splitting of Fe(III) within the samples increases slightly with the extent of iron oxidation (**Fig. 10**), which contrasts with the invariance of Fe(III) quadrupole splitting observed in prior work on natural oxidized trioctahedral smectites (Kohyama et al., 1973) and across trioctahedral phyllosilicates natively containing Fe(III) (Heller-Kallai and Rozenson, 1981).

4.2. Controls on the Extent and Rate of Oxidation by Dissolved Oxygen

Among the two compositions used in our study, the high-iron smectite exhibited a greater portion of the most reactive Fe(II) species and less nonreactive Fe(II) relative to the moderate-iron smectite. This behavior aligns with observations of reduced dioctahedral smectites, where neighboring cations impact the oxidation rates of Fe(II) and trioctahedral Fe(II)-Fe(II)-Fe(II) clusters show the greatest reactivity (Neumann et al., 2011). The greater iron content in the octahedral sheet of the high-iron smectite should result in a greater number of neighboring iron clusters in the absence of any ordering among octahedral sheet cations.

Changes in iron redox potential across different octahedral sites with different neighboring cations within the smectite may also contribute to the observed kinetic behavior and recalcitrant Fe(II) pool. Iron in dioctahedral smectites displays a non-Nernstian redox potential which varies alongside a variety of structural parameters (Gorski et al., 2012; Gorski et al., 2013). The underlying cause of this behavior is not fully known but may be due to either non-unity activity for different iron species or changes in the variety of local coordination environments that iron exists in within the smectite structure. This non-Nernstian redox behavior has been shown to effect the kinetics of U(VI) reduction by Fe(III) in a nontronite (Luan et al., 2014), resulting in a fast-reacting iron fraction, a slower fraction, and a non-reactive fraction. The exact potentials are dependent upon the specific smectite but studies of reduced dioctahedral smectites have not measured potentials positive enough to inhibit oxidation by oxygen (Gorski et al., 2012; Gorski et al., 2013). In addition, reduced dioctahedral smectites are observed to completely re-oxidize in air (Komadel et al., 1990; Komadel et al., 1995; Ribeiro et al., 2009; Stucki, 2011). The range of redox potentials for iron in trioctahedral ferrous smectites remains unexamined, but the incomplete extent of oxidation observed in this study suggests that these sites also have non-Nernstian redox potentials, and that these potentials may be shifted towards higher voltages.

Non-Nernstian redox potentials in smectites, however, may not explain the variation in extent of oxidation observed for each smectite under different oxygen concentrations. The differences in the concentrations investigated in this study only have minor effects on the redox potential (~0.015 V variation for the O_2/H_2O couple). Considering the redox potential behavior displayed by reduced dioctahedral smectites (Gorski et al., 2013), this small variation in oxidant redox potential would result in <2% difference in the fraction of Fe(II) oxidized, whereas the experiments reveal a 7% difference for the high-iron smectite and a 19% difference for the moderate-iron smectite. The differences in the extent of oxidation thus unlikely reflect thermodynamic effects. It is possible that there is a path dependence to the oxidation process in trioctahedral smectite, with more rapid initial oxidation caused by higher oxygen availability resulting in a larger portion of iron being accessible for oxidation. Slower oxidation may enable a mechanism to stabilize structural Fe(II), such as deprotonation of hydroxyl sites, migration of interlayer layers to offset charge, or interconversion of Fe(II) and Fe(III) sites through electron transfer (Neumann et al., 2008), to outcompete the consumption of Fe(II) sites through reaction with oxygen. The size of the recalcitrant iron pool may thus record the rate of oxidation and thus serve as an indirect proxy for oxygen concentration. This could be further evaluated through oxidation rate measurements at lower oxygen partial pressures.

Physical processes are unlikely to be responsible for the observed reaction rates of iron oxidation or explain the multiple species used in the model presented here. Application of the Scherrer equation to the (06,33) *hk* band estimates a ~130 Å coherent scattering domain size for the high-iron smectite and ~150 Å for the moderate-iron smectite. While these estimates may have substantial systematic errors given the composite nature of the (06,33) band, these values are consistent with prior studies of synthetic smectites which report platelets 100 to 200 Å in diameter (Farmer et al., 1994; Grauby et al., 1993; Lantenois et al., 2008; Zhang et al., 2019). It is unlikely that mass transfer limitations are the cause of slow kinetics in the studies presented here given the well mixed suspensions, the 432 to 674 h reaction time for the studies involving dissolved oxygen, and the small particle size of synthetic smectites. While edge sites may potentially react faster because they do not require electron transfer through the structure, their abundance is likely inadequate to explain the size of the fast-reacting Fe(II) pool (**Table 5**). Assuming a regular hexagonal particle morphology (see **Supplementary Material**), edge sites constitute too small of a fraction of total sites for particle >100 Å in size (**Fig. S4**). While the moderate-iron smectite in 2% oxygen had a small fast-reacting component that could be consistent with edge site oxidation, this experiment had a lower initial fractional Fe(II) content at and likely experienced partial Fe(II) oxidation during experiment initiation, consuming a portion of the fast-reacting Fe(II) pool. In other experiments, the portion of fast reacting iron ranged from 30% to 48%, which would require very small platelet diameter (<40 Å) or irregularly shaped crystals, inconsistent with the expected morphology and size of the synthetic smectite (Farmer et al., 1994; Grauby et al., 1993; Lantenois et al., 2008; Zhang et al., 2019).

4.3. Limited Reactivity of Structural Fe(II) with Nitrite

Over the time period examined in this study (650 h), nitrite did not detectably oxidize the iron present in the moderate-iron smectite. A small degree of oxidation was observed in the high-iron smectite: 17±4% after 1302 hours (**Fig. 4**). Note that this experiment was conducted for a substantially longer duration than studies of the same smectite in the air-equilibrated and microoxic studies (432 to 650 hours) in order to observe this partial oxidation. When comparing over the same reaction times, 10% of the Fe(II) in high-iron smectite exposed to nitrite oxidized compared to 78% and 60% in the air-equilibrated and micro-oxic samples, respectively. This demonstrates that although nitrite was present at ~20 times the maximum dissolved oxygen concentration used in this study it oxidizes Fe(II) in trioctahedral smectites at a far slower rate.

Minimal abiotic oxidation of Fe(II) in a reduced nontronite by nitrite was observed under neutral pH conditions during a 17 d (408 h) growth period (Zhao et al., 2013). This is largely consistent with our observations of no detectable oxidation in the moderate-iron smectite and oxidation within error of the oxidant-free control on a similar timescale for the high-iron smectite (**Fig. 4**). A separate study observed substantial abiotic nitrite reduction in the presence of reduced nontronite over ~300 h reaction period (Grabb et al., 2017). Those studies employed a large excess of clay Fe(II) relative to nitrite (32.9 mM Fe(II) versus 0.13 mM nitrite) whereas the present work utilized nitrite in stoichiometric excess (~1 mM Fe(II) versus 5 mM nitrite). This enabled rate determination via nitrite consumption, producing rate constants of 0.003 to 0.005 h^{-1} for reaction with reduced nontronite (Grabb et al., 2017) versus 0.0009±0.0008 h^{-1} was for the high-iron trioctahedral smectite and an unmeasurable rate for the moderate-iron smectite (**Table S2**). This suggests that natively Fe(II)-bearing trioctahedral smectites react substantially slower with nitrite then reduced, and originally Fe(III)-bearing, dioctahedral smectites.

4.4. Implications for Biogeochemical Iron Cycling

The retention of Fe(III) in the mineral structure following oxidation suggest that authigenic, trioctahedral Fe(II) smectites may be capable of repeated oxidation-reduction cycles in the same manner as nontronite and other Fe(III)-bearing smectites (Fialips et al., 2002a; Komadel et al., 1990; Komadel et al., 1995; Manceau et al., 2000a; Manceau et al., 2000b; Zhao et al., 2015). However, unlike dioctahedral smectites, the trioctahedral smectites in this study only partially oxidized upon prolonged exposure to oxygen, suggesting that not all iron in the structure is accessible to redox cycling. Long oxidizing periods may also affect such redox cycling because the excess positive charge produced following oxidation may drive eventual conversion to other products. A prior study (Chemtob et al., 2017) exposed similar smectites to dissolved oxygen for 6 d, hydrothermally recrystallized the products at 200°C, and then carried out a second oxidation cycle. Recrystallization increased the susceptibility towards oxidation, which may indicate that post-oxidation structural resetting would alter the extent of redox cycling possible. Hydrothermal treatment did not generate any new phyllosilicates and a smectite structure was preserved, although hematite formed during heating of a partially-oxidize iron-rich smectite (Chemtob et al., 2017). The rate of restructuring of oxidized trioctahedral smectites at non-hydrothermal temperatures is unclear and relatively rapid redox cycling may be able to proceed without the clay structure being substantially altered.

The rate of abiotic oxidation of trioctahedral Fe(II) smectite suggests that these phases represent potential electron donors for microorganisms. Recent work (Zhou et al., 2022) has shown that one of the trioctahedral smectites from the present study was able to support the growth of a microaerophilic Fe(II)-oxidizing bacterium. The rate of microbial oxidation was not always faster than abiotic oxidation in the same system but the organism expressed outer membrane proteins capable of conducting electron transfer with minerals only when grown on smectites and not with dissolved Fe(II), consistent with microbial utilization of smectite Fe(II). Access to the recalcitrant Fe(II) pool observed in the present work could not be investigated because the organism used loses viability beyond 15 d of incubation. Future work should evaluate whether a pre-oxidized smectite containing only recalcitrant Fe(II) can be further oxidized by microaerophilic Fe(II)-oxidizing bacteria as this will determine the size of the smectite Fe(II) pool accessible as an electron donor.

Irrespective of the accessibility of the recalcitrant Fe(II) pool, a series of studies now indicate that structural Fe(II) in smectites and other phyllosilicates is accessible to microbial oxidation under microaerophilic conditions (Benzine et al., 2013; Shelobolina et al., 2012b; Zhou et al., 2022). Such microbially-mediated oxidation may be pervasive in altered oceanic crust where ferrous smectites frequently coat cracks and vesicles (Alt and Teagle, 2003; Andrews, 1980; Colwell and D'Hondt, 2013). In addition, this larger Fe(II) pool may have served as a crustal redox buffer in oceanic basins on the early Earth. In addition, detrital Fe(II)-bearing smectites (Hao et al., 2017) may have provided a regular electron donor source to microoxic oases predicted to have transiently occurred in surface waters prior to the great oxidation event (Canfield, 2005; Riding et al., 2014) even after dissolved Fe(II) was consumed.

The exceedingly slow reaction of Fe(II)-bearing trioctahedral smectites with nitrite indicate that these phases are promising potentially electron donors for iron oxidizing, nitrate reducing bacteria. These phases undergo abiotic reaction with this intermediate nitrogen species substantially slower than reduced, dioctahedral smectites (Grabb et al., 2017). It is thus unclear whether oxidation of reduced nontronites by nitrate reducers (Benzine et al., 2013; Shelobolina et al., 2003; Shelobolina et al., 2012b) accurately predicts the ability of these organisms to utilize trioctahedral ferrous smectites. A study using the trioctahedral, Fe(II)-bearing mica biotite does indicate that such organisms induce a small amount of oxidation during nitrate reduction (Shelobolina et al., 2012a). Substantially greater oxidation may be possible in trioctahedral smectites because the high crystallinity and larger particle size of biotite should limit reactivity of that mineral.

Preservation in the rock record of natively trioctahedral smectites that have undergone redox cycling may result in uncertain signatures. Retention of Fe(III) in the clay structure would prevent iron isotope fractionation, with this isotopic record reflecting either conditions during clay formation or recrystallization during later diagenesis or metamorphism. These phases may, however, leave distinct mineralogical products compared to natively dioctahedral smectites. Iron reduction in dioctahedral smectites increases layer charge and can lead to eventual illitization (Jaisi et al., 2011; Kim et al., 2004; Koo et al., 2014). In contrast, iron oxidation in trioctahedral smectites decreases the layer charge of the smectite. Diagenesis or metamorphism may thus generate iron-rich talc, ferripyrophyllite, chlorite, or stilpnomelane from oxidized trioctahedral smectites.

5. CONCLUSIONS

Fe(II)-bearing trioctahedral smectites display different reactivity towards distinct oxidants. Nitrite induces minimal oxidation of structural Fe(II) while hydrogen peroxide, and thus likely reactive oxygen species, causes near-complete conversion to Fe(III). Abiotic reaction with dissolved oxygen, however, consistently leaves an unreactive Fe(II) pool in the smectite, even after nearly a month of oxidant exposure. This recalcitrance is supporting by kinetic modeling, which cannot describe the time-dependent oxidation behavior without including a portion of Fe(II) that is unreactive. Both the reactivity towards oxidants and incomplete extent of Fe(II) oxidation displayed by trioctahedral smectites are distinct behaviors from reduced dioctahedral smectites, indicating the role of mineral structure in controlling the redox behavior of iron-bearing phases.

The Fe(III) generated during oxidation remains in the clay structure, suggesting that trioctahedral smectites may be capable of redox cycling. The rates of abiotic oxidation indicate that these minerals represent potential electron donors for microaerophilic iron oxidizing and iron-oxidizing, nitrate-reducing bacteria. It is currently unclear whether the chemically-recalcitrant Fe(II) pool is available for biological utilization. Trioctahedral, Fe(II)-bearing smectites may have been important components of the iron biogeochemical cycle during the progressive oxidation of the surface of the Earth and potentially serve as redox buffers in altered oceanic crust. The impact of iron redox changes on layer charge in trioctahedral smectites suggests that diagenesis or metamorphism will leave mineral products in the rock record that are distinct from natively dioctahedral smectites.

ACKNOWLEDGEMENTS

This project was supported by the U.S. National Aeronautics and Space Administration (NASA) Exobiology Program through award no. 80NSSC18K129. Additional support was provided by the McDonnell Center for the Space Sciences at Washington University and by the NASA Astrobiology program through award no. 80NSSC19M0069. The authors thank Paul Carpenter for assistance with XRD measurements and Elaine Flynn for assistance with ICP-OES measurements and anaerobic chamber maintenance.

RESEARCH DATA

Research Data associated with this article can be accessed at https://doi.org/10.17632/8j3v4s9bs8.1

APPENDIX A. SUPPLEMENTARY MATERIAL

The Supplementary Material document contains full details of the media composition, time-series data for dissolved oxygen concentrations and temperature during the oxidation experiments investigating O_2, dissolved nitrite concentrations during the experiment with the moderate-iron smectite, kinetic fitting results for the nitrite and oxidant-free control experiments, and a calculation of the portion of total octahedral sites present at sheet edges as a function of particle size.

REFERENCES

Alt J. C. (1999) Very low-grade hydrothermal metamorphism of basic igneous rocks. In *Low-Grade Metamorphism* (eds. M. Frey and D. Robinson). Blackwell Publishing, Oxford. pp. 169-201.

Alt J. C. and Teagle D. A. H. (2003) Hydrothermal alteration of upper oceanic crust formed at a fast-spreading ridge: mineral, chemical, and isotopic evidence from ODP Site 801. *Chem. Geol.* **201**, 191-211.

Alt J. C., Honnorez J., Laverne C. and Emmermann R. (1986) Hydrothermal alteration of a 1 km section through the upper oceanic crust, Deep Sea Drilling Project Hole 504B: Mineralogy, chemistry and evolution of seawater-basalt interactions. *J. Geophys. Res.* **91**, 309-335.

Amonette J. E. (1994) *Quantitative methods in soil mineralogy*. Soil Science Society of America, Madison.

Andrews A. J. (1980) Saponite and celadonite in layer 2 basalts, DSDP Leg 37. *Contrib. Mineral. Petrol.* **73**, 323-340.

Andrews A. J., Dollase W. A. and Fleet M. E. (1983) A Mössbauer study of saponite in layer 2 basalt, Deep Sea Drilling Project Leg 69. *Initial Rep. Deep Sea Drill. Project* **69**, 585-588.

April R. H. and Keller D. M. (1992) Saponite and vermiculite in amygdales of the Granby Basaltic Tuff, Connecticut Valley. *Clays Clay Miner.* **40**, 22-31.

Babechuk M. G., Weimar N. E., Kleinhanns I. C., Eroglu S., Swanner E. D., Kenny G. G., Kamber B. S. and Schoenberg R. (2019) Pervasively anoxic surface conditions at the onset of the Great Oxidation Event: New multi-proxy constraints from the Cooper Lake paleosol. *Precambrian Res.* **323**, 126-163.

Badaut D., Besson G., Decarreau A. and Rautureau R. (1985) Occurrence of a ferrous, trioctahedral smectite in Recent sediments of Atlantis II Deep, Red Sea. *Clay Miner.* **20**, 389-404.

Baldermann A., Dohrmann R., Kaufhold S., Nickel C., Letofsky-Papst I. and Dietzel M. (2014) The Fe-Mg-saponite solid solution series–a hydrothermal synthesis study. *Clay Miner.* **49**, 391-415.

Ballet O., Coey J. M. D. and Burke K. J. (1985) Magnetic properties of sheet silicates; 2:1:1 layer minerals. *Phys. Chem. Miner.* **12**, 370-378.

Baron F., Petit S., Pentrák M., Decarreau A. and Stucki J. W. (2017) Revisiting the nontronite Mössbauer spectra. *Am. Mineral.* **102**, 1501-1515.

Benzine J., Shelobolina E., Xiong M. Y., Kennedy D. W., McKinley J. P., Lin X. J. and Roden E. E. (2013) Fe-phyllosilicate redox cycling organisms from a redox transition zone in Hanford 300 Area sediments. *Front. Microbiol.* **4**, 388.

Betlach M. R. and Tiedje J. M. (1981) Kinetic explanation for accumulation of nitrite, nitric oxide, and nitrous oxide during bacterial denitrification. *Appl. Environ. Microbiol.* **42**, 1074-1084.

Brown G. (1982) *Crystal structures of clay minerals and their X-ray identification*. Mineralogical Society, London.

Canfield D. E. (2005) The early history of atmospheric oxygen: homage to Robert M. Garrels. *Annu. Rev. Earth Planet. Sci.* **33**, 1-36.

Canfield D. E., Poulton S. W. and Narbonne G. M. (2007) Late-Neoproterozoic deep-ocean oxygenation and the rise of animal life. *Science* **315**, 92-95.

Cardile C. M., Johnston J. H. and Dickson D. P. E. (1986) Magnetic Ordering At 4.2 And 1.3 K in Nontronites of Different Iron Contents: A ^{57}Fe Mössbauer Spectroscopic Study. *Clays Clay Miner.* **34**, 233-238.

Chemtob S. M., Nickerson R. D., Morris R. V., Agresti D. G. and Catalano J. G. (2015) Synthesis and structural characterization of ferrous trioctahedral smectites: Implications for clay mineral genesis and detectability on Mars. *J. Geophys. Res.: Planets* **120**, 1119-1140.

Chemtob S. M., Nickerson R. D., Morris R. V., Agresti D. G. and Catalano J. G. (2017) Oxidative alteration of ferrous smectites and implications for the redox evolution of early Mars. *J. Geophys. Res.: Planets* **122**, 2469-2488.

Chen C., Kukkadapu R. K., Lazareva O. and Sparks D. L. (2017) Solid-phase Fe speciation along the vertical redox gradients in floodplains using XAS and Mössbauer spectroscopies. *Environ. Sci. Technol.* **51**, 7903-7912.

Chen C., Meile C., Wilmoth J., Barcellos D. and Thompson A. (2018) Influence of pO_2 on iron redox cycling and anaerobic organic carbon mineralization in a humid tropical forest soil. *Environ. Sci. Technol.* **52**, 7709-7719.

Colwell F. S. and D'Hondt S. (2013) Nature and extent of the deep biosphere. *Rev. Mineral. Geochem.* **75**, 547-574.

Craw D., Smith D. W. and Youngson J. H. (1995) Formation of authigenic Fe^{2+}-bearing smectite-vermiculite during terrestrial diagenesis, southern New Zealand. *N. Z. J. Geol. Geophys.* **38**, 151-158.

Decarreau A. and Bonnin D. (1986) Synthesis and crystallogenesis at low-temperature of Fe(III)-smectites by evolution of coprecipitated gels - experiments in partially reducing conditions. *Clay Miner.* **21**, 861-877.

Drits V. A. and Manceau A. (2000) A model for the mechanism of Fe^{3+} to Fe^{2+} reduction in dioctahedral smectites. *Clays Clay Miner.* **48**, 185-195.

Dyar M. D., Schaefer M. W., Sklute E. C. and Bishop J. L. (2008) Mössbauer spectroscopy of phyllosilicates: Effects of fitting models on recoil-free fractions and redox ratios. *Clay Miner.* **43**, 3-33.

Ehlmann B. L., Hodyss R., Bristow T. F., Rossman G. R., Ammannito E., De Sanctis M. C. and Raymond C. A. (2018) Ambient and cold-temperature infrared spectra and XRD patterns of ammoniated phyllosilicates and carbonaceous chondrite meteorites relevant to Ceres and other solar system bodies. *Meteorit. Planet. Sci.* **53**, 1884-1901.

Emerson D. and Merrill Floyd M. (2005) Enrichment and isolation of iron-oxidizing bacteria at neutral pH. In *Methods in Enzymology, Volume 397* (ed. J. R. Leadbetter). Academic Press. pp. 112-123.

Evans R. J., Rancourt D. G. and Grodzicki M. (2005) Hyperfine electric field gradients and local distortion environments of octahedrally coordinated Fe^{2+}. *Am. Mineral.* **90**, 187-198.

Farmer V. C., McHardy W. J., Elsass F. and Robert M. (1994) *hk*-ordering in aluminous nontronite and saponite synthesized near 90° C: Effects of synthesis conditions on nontronite composition and ordering. *Clays Clay Miner.* **42**, 180-186.

Fialips C. I., Huo D., Yan L. B., Wu J. and Stucki J. W. (2002a) Infrared study of reduced and reduced-reoxidized ferruginous smectite. *Clays Clay Miner.* **50**, 455-469.

Fialips C. I., Huo D. F., Yan L. B., Wu J. and Stucki J. W. (2002b) Effect of Fe oxidation state on the IR spectra of Garfield nontronite. *Am. Mineral.* **87**, 630-641.

Fox V. K., Kupper R. J., Ehlmann B. L., Catalano J. G., Razzell-Hollis J., Abbey W. J., Schild D. J., Nickerson R. D., Peters J. C. and Katz S. M. (2021) Synthesis and characterization of Fe(III)-Fe(II)-Mg-Al smectite solid solutions and implications for planetary science. *Am. Mineral.* **106**, 964-982.

Glass C. and Silverstein J. (1998) Denitrification kinetics of high nitrate concentration water: pH effect on inhibition and nitrite accumulation. *Water Res.* **32**, 831-839.

Gorski C. A., Klüpfel L. E., Voegelin A., Sander M. and Hofstetter T. B. (2012) Redox properties of structural Fe in clay minerals. 2. Electrochemical and spectroscopic characterization of electron transfer irreversibility in ferruginous smectite, SWa-1. *Environ. Sci. Technol.* **46**, 9369-9377.

Gorski C. A., Klüpfel L. E., Voegelin A., Sander M. and Hofstetter T. B. (2013) Redox properties of structural Fe in clay minerals. 3. Relationships between smectite redox and structural properties. *Environ. Sci. Technol.* **47**, 13477-13485.

Grabb K. C., Buchwald C., Hansel C. M. and Wankel S. D. (2017) A dual nitrite isotopic investigation of chemodenitrification by mineral-associated Fe(II) and its production of nitrous oxide. *Geochim. Cosmochim. Acta* **196**, 388-402.

Grauby O., Petit S., Decarreau A. and Baronnet A. (1993) The beidellite-saponite series: an experimental approach. *Eur. J. Mineral.* **5**, 623-636.

Hao J., Sverjensky D. A. and Hazen R. M. (2017) A model for late Archean chemical weathering and world average river water. *Earth Planet. Sci. Lett.* **457**, 191-203.

Heller-Kallai L. and Rozenson I. (1981) The use of Mössbauer spectroscopy of iron in clay mineralogy. *Phys. Chem. Miner.* **7**, 223-238.

Holland H. D. (2004) 6.21: The geologic history of seawater. In *Treatise on Geochemistry* (ed. H. Elderfield). Pergamon, Oxford. pp. 583-685.

Huggins F. E. (1976) Mössbauer studies of iron minerals under pressures of up to 200 kilobars. In *The Physics and Chemistry of Minerals and Rocks* (ed. R. G. J. Strens). Wiley, New York. pp. 613-640.

Ivanov V. M. (2004) The 125th Anniversary of the Griess Reagent. *J. Anal. Chem.* **59**, 1002-1005.

Jaisi D. P., Eberl D. D., Dong H. L. and Kim J. (2011) The formation of illite from nontronite by mesophilic and thermophilic bacterial reaction. *Clays Clay Miner.* **59**, 21-33.

Kappler A., Schink B. and Newman D. K. (2005) Fe(III) mineral formation and cell encrustation by the nitrate-dependent Fe(II)-oxidizer strain BoFeN1. *Geobiology* **3**, 235-245.

Khaled E. M. and Stucki J. W. (1991) Iron oxidation state effects on cation fixation in smectites. *Soil Sci. Soc. Am. J.* **55**, 550-554.

Kim J., Dong H. L., Seabaugh J., Newell S. W. and Eberl D. D. (2004) Role of microbes in the smectite-to-illite reaction. *Science* **303**, 830-832.

Klueglein N. and Kappler A. (2013) Abiotic oxidation of Fe(II) by reactive nitrogen species in cultures of the nitrate-reducing Fe(II) oxidizer *Acidovorax* sp BoFeN1 - questioning the existence of enzymatic Fe(II) oxidation. *Geobiology* **11**, 180-190.

Klueglein N., Zeitvogel F., Stierhof Y. D., Floetenmeyer M., Konhauser K. O., Kappler A. and Obst M. (2014) Potential role of nitrite for abiotic Fe(II) oxidation and cell encrustation during nitrate reduction by denitrifying bacteria. *Appl. Environ. Microbiol.* **80**, 1051-1061.

Kohyama N., Shimoda S. and Sudo T. (1973) Iron-rich saponite (ferrous and ferric forms). *Clays Clay Miner.* **21**, 229-237.

Komadel P., Lear P. R. and Stucki J. W. (1990) Reduction and reoxidation of nontronite: Extent of reduction and reaction rates. *Clays Clay Miner.* **38**, 203-208.

Komadel P., Madejova J. and Stucki J. W. (1995) Reduction and reoxidation of nontronite: Questions of reversibility. *Clays Clay Miner.* **43**, 105-110.

Komadel P., Madejova J. and Stucki J. W. (1999) Partial stabilization of Fe(II) in reduced ferruginous smectite by Li fixation. *Clays Clay Miner.* **47**, 458-465.

Komadel P., Madejová J. and Bujdák J. (2005) Preparation and properties of reduced-charge smectites – A review. *Clays Clay Miner.* **53**, 313-334.

Koo T.-H., Jang Y.-N., Kogure T., Kim J. H., Park B. C., Sunwoo D. and Kim J.-W. (2014) Structural and chemical modification of nontronite associated with microbial Fe(III) reduction: Indicators of "illitization". *Chem. Geol.* **377**, 87-95.

Kristmannsdottir H. (1979) Alteration of basaltic rocks by hydrothermal-activity at 100-300°C. In *International Clay Conference 1978* (eds. M. M. Mortland and V. C. Farmer). Elsevier, Amsterdam. pp. 359-367.

Lagarec K. and Rancourt D. G. (1997) Extended Voigt-based analytic lineshape method for determining N-dimensional correlated hyperfine parameter distributions in Mössbauer spectroscopy. *Nucl. Instrum. Methods Phys. Res., Sect. B* **129**, 266-280.

Lantenois S., Champallier R., Bény J.-M. and Muller F. (2008) Hydrothermal synthesis and characterization of dioctahedral smectites: A montmorillonites series. *Appl. Clay Sci.* **38**, 165-178.

Luan F., Gorski C. A. and Burgos W. D. (2014) Thermodynamic controls on the microbial reduction of iron-bearing nontronite and uranium. *Environ. Sci. Technol.* **48**, 2750-2758.

Lyons T. W., Reinhard C. T. and Planavsky N. J. (2014) The rise of oxygen in Earth's early ocean and atmosphere. *Nature* **506**, 307-315.

Manceau A., Lanson B., Drits V. A., Chateigner D., Gates W. P., Wu J., Huo D. and Stucki J. W. (2000a) Oxidation-reduction mechanism of iron in dioctahedral smectites: I. Crystal chemistry of oxidized reference nontronites. *Am. Mineral.* **85**, 133-152.

Manceau A., Drits V. A., Lanson B., Chateigner D., Wu J., Huo D., Gates W. P. and Stucki J. W. (2000b) Oxidation-reduction mechanism of iron in dioctahedral smectites: II. Crystal chemistry of reduced Garfield nontronite. *Am. Mineral.* **85**, 153-172.

Moore D. M. and Reynolds R. C. (1997) *X-Ray Diffraction and the Identification and Analysis of Clay Minerals*, 2nd ed. Oxford University Press, New York.

Murad E. and Cashion J. (2004) *Mössbauer Spectroscopy of Environmental Materials and Their Industrial Utilization* Kluwer Academic Publishers, Norwell, Massachusetts.

Neumann A., Petit S. and Hofstetter T. B. (2011) Evaluation of redox-active iron sites in smectites using middle and near infrared spectroscopy. *Geochim. Cosmochim. Acta* **75**, 2336-2355.

Neumann A., Hofstetter T. B., Lussi M., Cirpka O. A., Petit S. and Schwarzenbach R. P. (2008) Assessing the redox reactivity of structural iron in smectites using nitroaromatic compounds as kinetic probes. *Environ. Sci. Technol.* **42**, 8381-8387.

Neveu M., Desch S. J. and Castillo-Rogez J. C. (2017) Aqueous geochemistry in icy world interiors: Equilibrium fluid, rock, and gas compositions, and fate of antifreezes and radionuclides. *Geochim. Cosmochim. Acta* **212**, 324-371.

Noor N. and Thompson A. (2022) Localized alteration of ferrihydrite natural organic matter coprecipitates following reaction with Fe(II). *Soil Sci. Soc. Am. J.* **86**, 253-263.

Parthasarathy G., Choudary B. M., Sreedhar B., Kunwar A. C. and Srinivasan R. (2003) Ferrous saponite from the Deccan Trap, India, and its application in adsorption and reduction of hexavalent chromium. *Am. Mineral.* **88**, 1983-1988.

Pentráková L., Su K., Pentrák M. and Stucki J. W. (2013) A review of microbial redox interactions with structural Fe in clay minerals. *Clay Miner.* **48**, 543-560.

Rancourt D. G. (1994a) Mössbauer spectroscopy of minerals II. Problem of resolving cis and trans octahedral Fe^{2+} sites. *Phys. Chem. Miner.* **21**, 250-257.

Rancourt D. G. (1994b) Mössbauer spectroscopy of minerals: I. Inadequacy of Lorentzian-line doublets in fitting spectra arising from quadrupole splitting distributions. *Phys. Chem. Miner.* **21**, 244-249.

Rancourt D. G., Christie I. A. D., Lamarche G., Swainson I. and Flandrois S. (1994) Magnetism of synthetic and natural annite mica: ground state and nature of excitations in an exchange-wise two-dimensional easy-plane ferromagnet with disorder. *J. Magn. Magn. Mater.* **138**, 31-44.

Ribeiro F. R., Fabris J. D., Kostka J. E., Komadel P. and Stucki J. W. (2009) Comparisons of structural iron reduction in smectites by bacteria and dithionite: II. A variable-temperature Mössbauer spectroscopic study of Garfield nontronite. *Pure Appl. Chem.* **81**, 1499-1509.

Riding R., Fralick P. and Liang L. (2014) Identification of an Archean marine oxygen oasis. *Precambrian Res.* **251**, 232-237.

Rivkin A. S., Volquardsen E. L. and Clark B. E. (2006) The surface composition of Ceres: Discovery of carbonates and iron-rich clays. *Icarus* **185**, 563-567.

Rothwell K. A. (2019) From the lab to the real world: The redox reactivity of Fe-bearing clay minerals in complex biogeochemical environments. Ph.D. Dissertation Newcastle University.

Sakuma H., Morida K., Takahashi Y., Fukushi K., Noda N., Sekine Y. and Tamura K. (2022) Synthesis of ferrian and ferro-saponites: Implications for the structure of (Fe,Mg)-smectites formed under reduced conditions. *Am. Mineral.* **107**, 1926-1935.

Shannon R. D. (1976) Revised effective ionic radii and systematic studies of interatomic distances in halides and chalcogenides. *Acta Crystallogr.* **A32**, 751-767.

Shelobolina E., Xu H., Konishi H., Kukkadapu R., Wu T., Blöthe M. and Roden E. (2012a) Microbial lithotrophic oxidation of structural Fe(II) in biotite. *Appl. Environ. Microbiol.* **78**, 5746-5752.

Shelobolina E. S., Vanpraagh C. G. and Lovley D. R. (2003) Use of ferric and ferrous iron containing minerals for respiration by *Desulfitobacterium frappieri*. *Geomicrobiol. J.* **20**, 143-156.

Shelobolina E. S., Konishi H., Xu H., Benzine J., Xiong M. Y., Wu T., Blöthe M. and Roden E. (2012b) Isolation of phyllosilicate-iron redox cycling microorganisms from an illite-smectite rich hydromorphic soil. *Front. Microbiol.* **3**, 134.

Shen S. and Stucki J. W. (1994) Effects of iron oxidation state on the fate and behavior of potassium in soils. In *Soil Testing: Prospects for Improving Nutrient Recommendations* (eds. J. L. Havlin and J. S. Jacobsen). Soil Science Society of America and American Society of Agronomy, Madison. pp. 173-185.

Shen S. Y., Stucki J. W. and Boast C. W. (1992) Effects of structural iron reduction on the hydraulic conductivity of Na-smectite. *Clays Clay Miner.* **40**, 381-386.

Shen Y., Canfield D. E. and Knoll A. H. (2002) Middle Proterozoic ocean chemistry: Evidence from the McArthur Basin, northern Australia. *Am. J. Sci.* **302**, 81-109.

Stucki J. W. (2011) A review of the effects of iron redox cycles on smectite properties. *C.R. Geosci.* **343**, 199-209.

Sun J., Mailloux B. J., Chillrud S. N., van Geen A., Thompson A. and Bostick B. C. (2018) Simultaneously quantifying ferrihydrite and goethite in natural sediments using the method of standard additions with X-ray absorption spectroscopy. *Chem. Geol.* **476**, 248-259.

Tarafder P. K. and Thakur R. (2013) An optimised 1,10-phenanthroline method for the determination of ferrous and ferric oxides in silicate rocks, soils and minerals. *Geostand. Geoanal. Res.* **37**, 155-168.

Teagle D. A. H., Alt J. C., Bach W., Halliday A. N. and Erzinger J. (1996) Alteration of upper ocean crust in a ridge-flank hydrothermal upflow zone: Mineral, chemical, and isotopic constraints from Hole 896A. *Proc. Ocean Drill. Program Part B Sci. Results* **148**, 119-150.

Treiman A. H., Morris R. V., Agresti D. G., Graff T. G., Achilles C. N., Rampe E. B., Bristow T. F., Ming D. W., Blake D. F. and Vaniman D. T. (2014) Ferrian saponite from the Santa Monica Mountains (California, USA, Earth): Characterization as an analog for clay minerals on Mars with application to Yellowknife Bay in Gale Crater. *Am. Mineral.* **99**, 2234-2250.

Vaniman D. T., Bish D. L., Ming D. W., Bristow T. F., Morris R. V., Blake D. F., Chipera S. J., Morrison S. M., Treiman A. H., Rampe E. B., Rice M., Achilles C. N., Grotzinger J. P., McLennan S. M., Williams J., Bell J. F., Newsom H. E., Downs R. T., Maurice S., Sarrazin P., Yen A. S., Morookian J. M., Farmer J. D., Stack K., Milliken R. E., Ehlmann B. L., Sumner D. Y., Berger G., Crisp J. A., Hurowitz J. A., Anderson R., Des Marais D. J., Stolper E. M., Edgett K. S., Gupta S., Spanovich N. and Team M. S. L. S. (2014) Mineralogy of a mudstone at Yellowknife Bay, Gale crater, Mars. *Science* **343**, 1243480.

Velde B. and Meunier A. (2008) *The Origin of Clay Minerals in Soils and Weathered Rocks*. Springer, Berlin, Heidelberg.

Watanabe T. and Sato T. (1988) Expansion characteristics of montmorillonite and saponite under various relative humidity conditions. *Clay Sci.* **7**, 129-138.

Weber K. A., Pollock J., Cole K. A., O'Connor S. M., Achenbach L. A. and Coates J. D. (2006) Anaerobic nitrate-dependent iron(II) bio-oxidation by a novel lithoautotrophic betaproteobacterium, strain 2002. *Appl. Environ. Microbiol.* **72**, 686-694.

Whitaker A. H., Austin R. E., Holden K. L., Jones J. L., Michel F. M., Peak D., Thompson A. and Duckworth O. W. (2021) The structure of natural biogenic iron (oxyhydr)oxides formed in circumneutral pH environments. *Geochim. Cosmochim. Acta* **308**, 237-255.

Zhang C., Petit S., He H., Villieras F., Razafitianamaharavo A., Baron F., Tao Q. and Zhu J. (2019) Crystal growth of smectite: A study based on the change in crystal chemistry and morphology of saponites with synthesis time. *ACS Earth Space Chem.* **4**, 14-23.

Zhao L., Dong H., Kukkadapu R. K., Zeng Q., Edelmann R. E., Pentrák M. and Agrawal A. (2015) Biological redox cycling of iron in nontronite and its potential application in nitrate removal. *Environ. Sci. Technol.* **49**, 5493-5501.

Zhao L. D., Dong H. L., Kukkadapu R., Agrawal A., Liu D., Zhang J. and Edelmann R. E. (2013) Biological oxidation of Fe(II) in reduced nontronite coupled with nitrate reduction by *Pseudogulbenkiania* sp. strain 2002. *Geochim. Cosmochim. Acta* **119**, 231-247.

Zhou N., Kupper R. J., Catalano J. G., Thompson A. and Chan C. S. (2022) Biological oxidation of Fe(II)-bearing smectite by microaerophilic Fe-oxidizer *Sideroxydans lithotrophicus* using dual Cyc2 and Mto Fe oxidation pathways. *Environ. Sci. Technol.* **56**, 17443–17453.

Table 1. Concentrations and volumes of each salt used in the initial precipitating solutions for the synthesis of the smectites used in this study.

Designation	**Target Fe:Mg:Al ratio**	**Final Fe:Mg:Al ratio**	**1 mol L^{-1} $FeCl_2$**	**1 mol L^{-1} $MgCl_2$**	**1 mol L-^{1} $AlCl_3$**	**0.5 mol L^{-1} Na_2SiO_3**
Moderate-Iron	40:40:20	53:24:23	10 mL	10 mL	5 mL	58.67 mL
High-Iron	60:20:20	70:08:23	15 mL	5 mL	5 mL	58.67 mL

Table 2. Structural formulae for the synthetic smectites used in this study with Fe(II)/Fe(Total) determined by Mössbauer spectroscopy.

Label	**Formula**	**Octahedral Occupancy**	**Fe(II) / Fe(Total)**	**Total Charge**	**O-Charge**	**T-Charge**
Moderate-Iron	$Ca_{0.17}(Fe^{II}_{1.59}Mg_{0.78}Fe^{III}_{0.12}Al_{0.33})(Si_{3.58}Al_{0.42})O_{10}(OH)_2$	2.82	0.94	-0.34	+0.08	-0.42
High-Iron	$Ca_{0.20}(Fe^{II}_{2.16}Mg_{0.26}Fe^{III}_{0.19}Al_{0.24})(Si_{3.48}Al_{0.52})O_{10}(OH)_2$	2.85	0.92	-0.40	+0.13	-0.52

Table 3. Fitting parameters of the 295 K Mössbauer spectra of the smectites before and after oxidant exposure.

Smectite	**Component**	**CS (mm/s)** [a]	**QS (mm/s)** [b]	**Area (%)**
Moderate-Iron				
	Ferric	0.45±0.03	0.40±0.05	8.1±0.8%
	Ferrous	1.130±0.003	2.614±0.005	92.0± 0.8%
High-Iron				
	Ferric	0.50±0.02	0.41±0.02	8.4±0.3%
	Ferrous	1.134±0.001	2.54±0.03	91.6±0.3%
Moderate-iron nitrite				
	Ferric	0.488±0.009	0.49±0.03	24.1±0.3%
	Ferrous	1.131±0.001	2.592±0.002	75.9±0.3%
High-iron nitrite				
	Ferric	0.43±0.01	0.79±0.02	49.0±0.6%
	Ferrous	1.120±0.006	2.53±0.01	51.0±0.6%
Moderate-iron 2% O_2				
	Ferric	0.37±0.01	0.80±0.02	57.7±0.7%
	Ferrous	1.122±0.002	2.56±0.02	42.3±0.7%
High-iron 2% O_2				
	Ferric	0.37±0.05	0.81±0.01	79.9±0.8%
	Ferrous	1.06±0.03	2.45±0.06	20.1±0.8%
Moderate-iron 21% O_2				
	Ferric	0.36±0.09	0.87±0.02	71.5±0.6%
	Ferrous	1.13±0.01	2.51±0.03	28.5±0.6%
High-iron 21% O_2				
	Ferric	0.353±0.008	0.85±0.01	86.0±0.6%
	Ferrous	1.13±0.04	2.33±0.07	14.0±0.6%
Moderate-iron H_2O_2				
	Ferric	0.351±0.003	0.996±0.005	93.7±0.4%
	Ferrous	1.14±0.02	2.42±0.03	6.3±0.4%
High-iron H_2O_2				
	Ferric	0.352±0.008	0.898±0.005	96.6±0.6%
	Ferrous	1.14±0.02	2.30±0.07	3.4±0.6%

[a] Chemical shift.

[b] Quadrupole splitting.

Table 4. Results of individual oxidation experiments.

Smectite	Oxidant	Initial pH	Final pH	Initial Colorimetric Smectite Fe(II)/Fe(Total)	Final Colorimetric Smectite Fe(II)/Fe(Total)	Final Mössbauer Smectite Fe(II)/Fe(Total)
Moderate-Iron	None	6.29±0.01[a]	6.70±0.02	83±3%	88±2%	84.3±0.5%
	21% O_2	6.16±0.01	6.98±0.02	81±1%	26±4%	28.5±0.6%
	2% O_2	6.20± 0.02	6.66±0.05	75±3%	43.4±0.4%	42.3±0.7%
	5 mmol $L^{-1}NO_2^-$	6.29± 0.08	6.73±0.01	85±4%	85±4%	75.9±0.3%
	H_2O_2	6.30± 0.02	-[b]	78±4%	6±3%	6.3±0.4%
High-Iron	None	6.18± 0.01	6.60±0.01	92±3%	93±3%	91.6±0.3%
	21% O_2	6.24± 0.02	7.11±0.02	92.4±0.8%	14.1± 0.2%	14.0±0.6%
	2% O_2	6.25± 0.01	6.68±0.06	89±1%	28.6±0.1%	20.1±0.8%
	5mM NO_2^-	6.26± 0.02	6.57±0.04	90±5%	73±4%	51.0±0.6%
	H_2O_2	6.26± 0.05	-	85±4%	5.3±0.5%	3.4±0.6%

[a] pH and colorimetric Fe(II)/Fe(Total) percentages are the average and standard deviation of measurements from triplicate samples. Mössbauer Fe(II)/Fe(Total) is the uncertainty in the fit of a single sample

[b] pH was not measured following H_2O_2 exposure

Table 5. Kinetic fit parameters for each of the oxygen exposure studies.

Smectite	**Oxidant**	**k_1 (h^{-1})** [a]	**a_1**	**k_2 (h^{-1})**	**a_2**	**Recalcitrant Fe(II) Fraction**	**Reduced χ^2** [b]
Moderate-Iron							
	21% O_2	2.58	0.30±0.02	0.07±0.01	0.29±0.01	0.22±0.02	1.82[b]
	2% O_2	0.47	0.06±0.03	0.10±0.07	0.27±0.01	0.41±0.01	2.10
High-Iron							
	21% O_2	2.6±0.4	0.48±0.02	0.040±0.007	0.36±0.02	0.091±0.009	1.66
	2% O_2	0.5±0.1	0.38±0.03	0.012±0.003	0.36±0.02	0.16±0.02	3.71

[a] Fitting parameters are as follows: k_1 is the rate constant of the first equation, a_1 is the portion of the ferrous iron that is governed by the first rate term, k_2 is the rate constant of the second equation, a_2 is the portion governed by the second rate term, and the recalcitrant fraction is the portion of Fe(II) that is assumed non-reactive by the model. Note the dependent variable being modeled is unitless (mole fraction) and thus does not contribute to the units for the rate constants.

[b] Reduced χ^2 is a goodness of fit parameter.

Table 6. Fitted (001) peak and (06,33) band positions and calculated d-space values.

Smectite	(001) position (°2θ)	d_{001} (Å)	(06,33) position (°2θ)	$d_{06,33}$ (Å)
Moderate-Iron				
Initial	5.45(2)[a]	16.2	60.163(8)	1.537
21% O_2	6.17(2)	14.3	60.509(6)	1.529
2% O_2	6.18(2)	14.3	60.41(1)	1.531
5 mmol L^{-1} NO_2^-	5.86(1)	15.1	60.247(9)	1.535
H_2O_2	6.42(2)	13.8	60.704(6)	1.524
High-Iron				
Initial	5.37(2)	16.4	59.787(5)	1.546
21% O_2	6.40(3)	13.8	60.619(8)	1.526
2% O_2	6.17(2)	14.3	60.434(9)	1.531
5 mmol L^{-1} NO_2^-	5.90(2)	15.0	60.071(6)	1.539
H_2O_2	6.19(2)	14.3	60.811(9)	1.522

[a] Values in parentheses represent the uncertainty in the last digit.

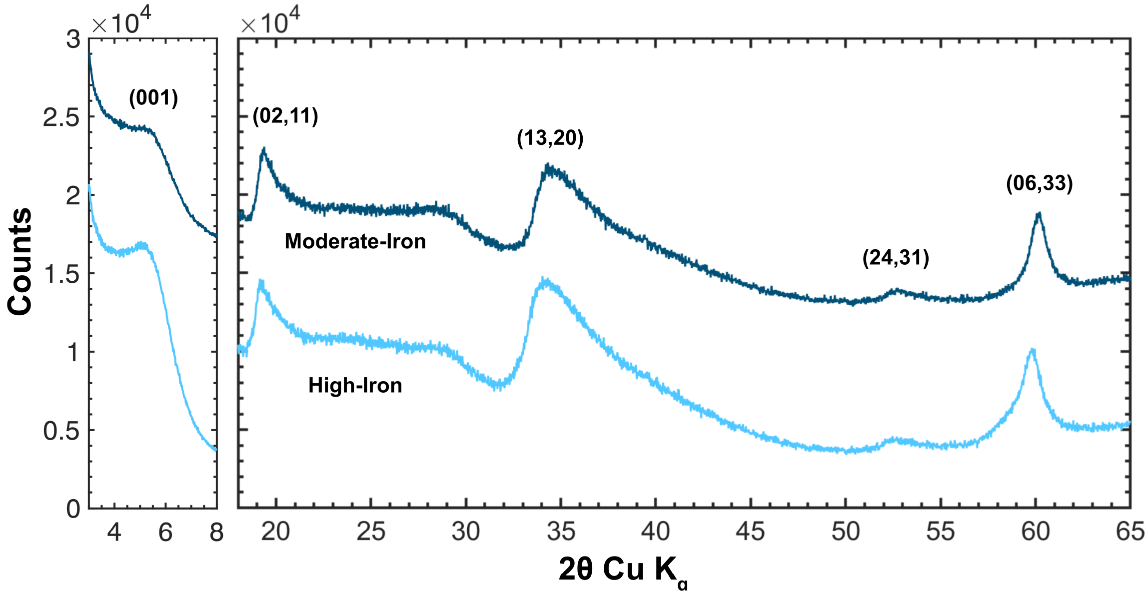

Figure 1. XRD patterns of the initial synthetic smectites. Patterns are offset vertically for clarity. Labels indicate major peaks and bands. Data between 8 and 18° is obsercured by a large scattering feature from the acrylic dome used to prevent oxidation and is thus not displayed.

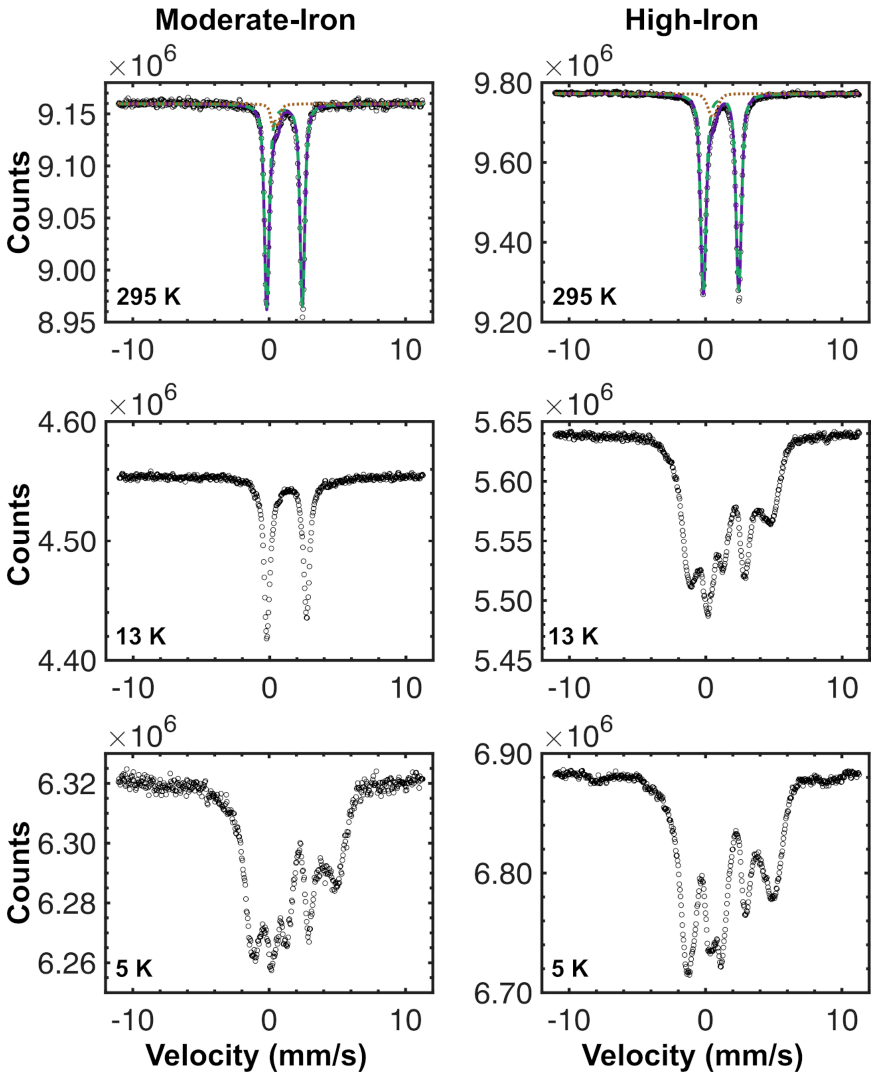

Figure 2. ^{57}Fe Mössbauer spectra of the synthetic smectites. Fits to the 295 K spectra in purple are the sum of ferrous and ferric components represented by dashed green and dotted brown lines, respectively.

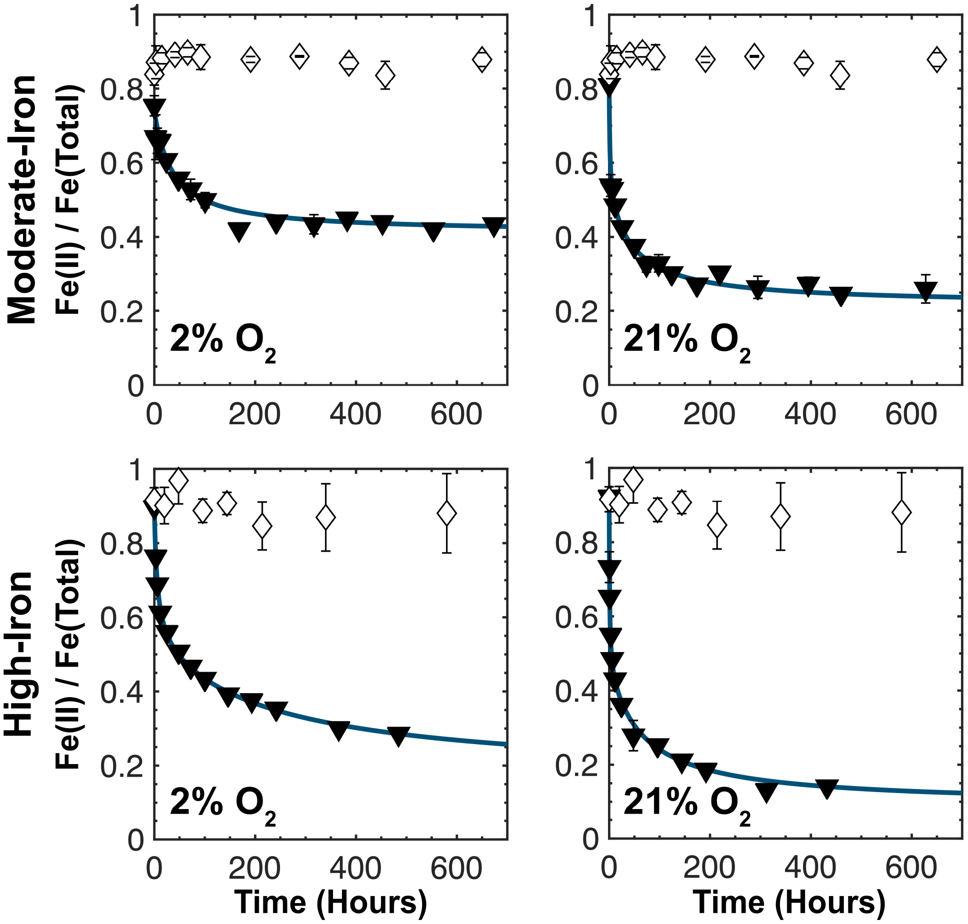

Figure 3. Fe(II)/Fe(Total) and modeled rates of oxidation for both smectite compositions (rows) exposed to oxygen at two different partial pressures (columns) compared with oxidant free control studies. Open diamonds are the oxidant-free control experiments, solid triangles are for the experiments using dissolved oxygen, and blue lines are the kinetic model fits.

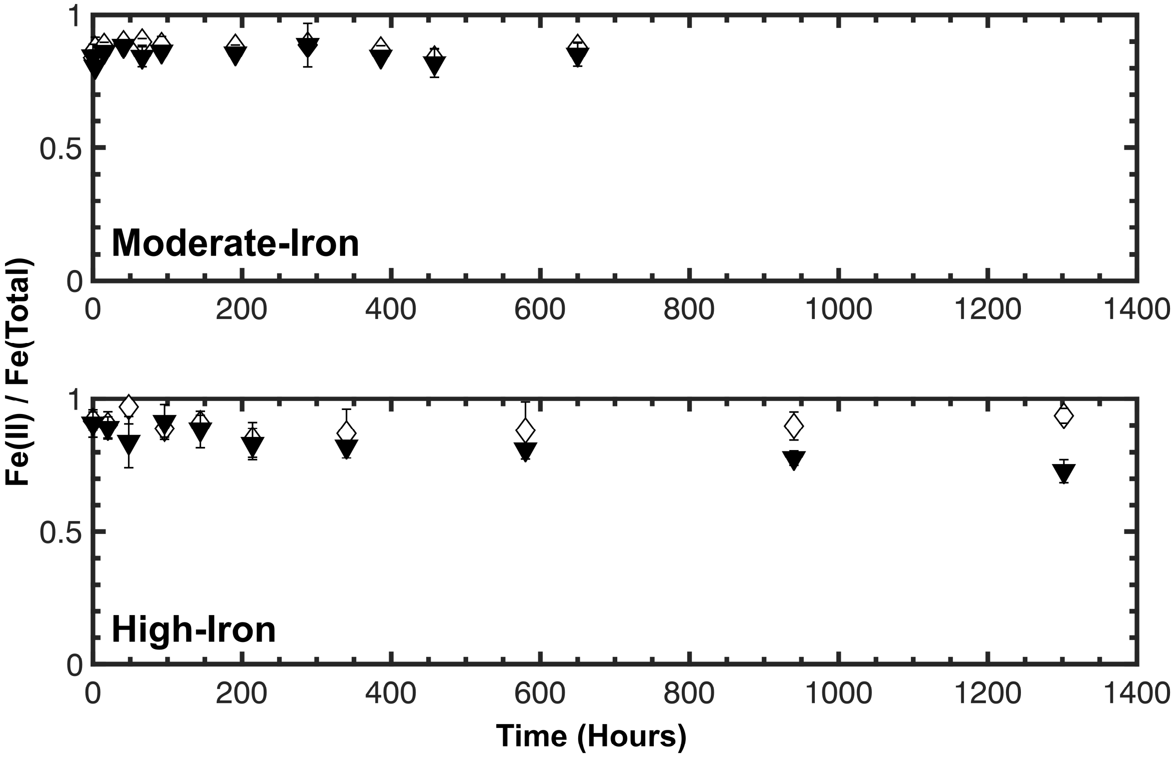

Figure 4. Fe(II)/Fe(Total) for both smectites exposed to 5 mmol L^{-1} nitrite compared with oxidant-free controls.

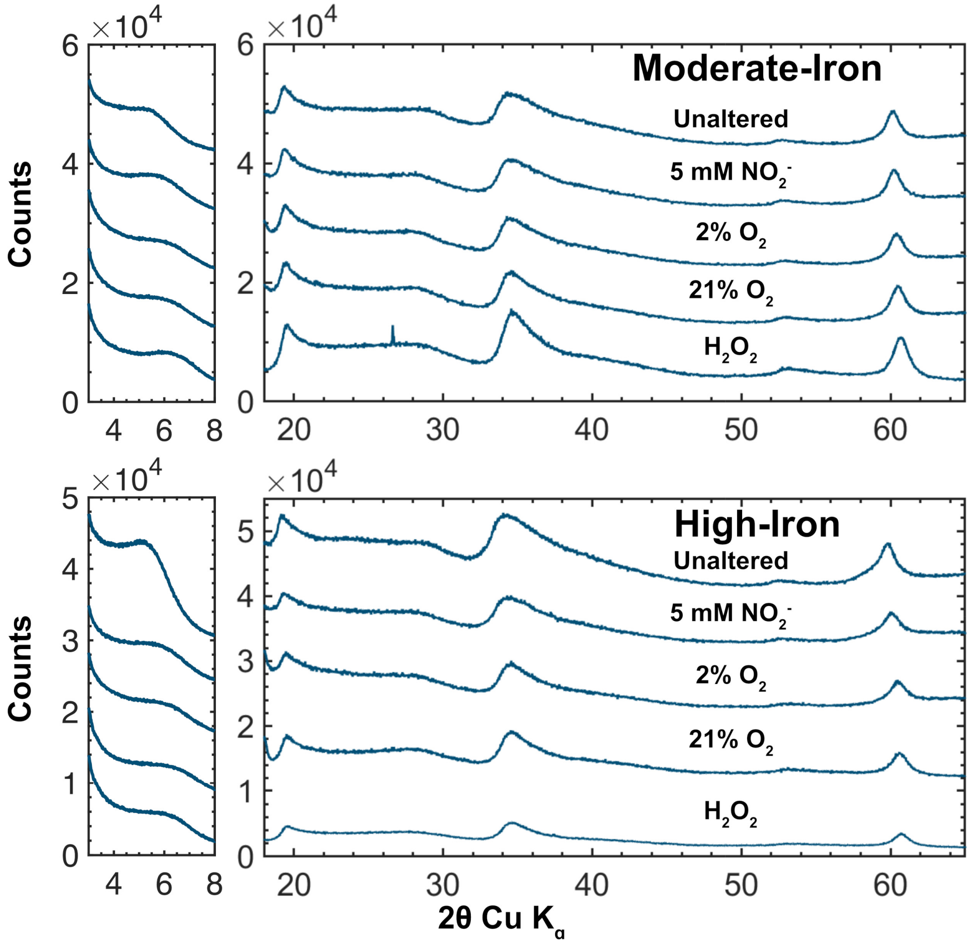

Figure 5. XRD patterns of each smectite and its oxidation products, vertically offset. The small sharp peak in the moderate-iron H_2O_2 pattern is from a quartz contaminant introduced during grinding.

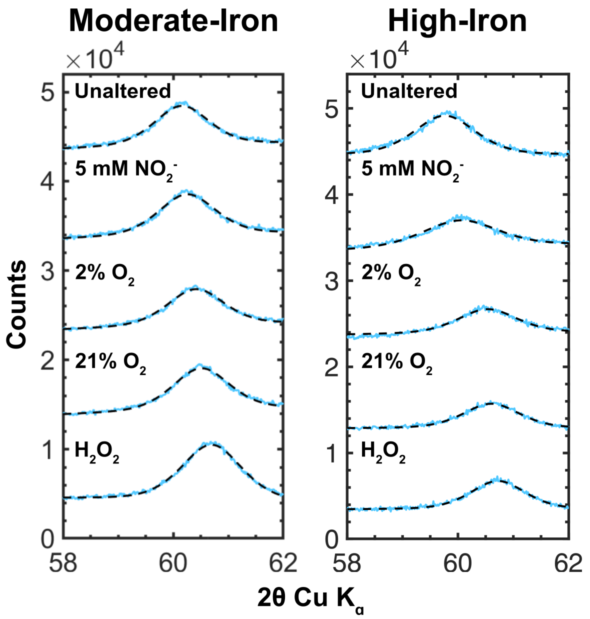

Figure 6. The (06,33) band in the XRD patterns (solid) and fitted peaks (dashed) of each smectite and its oxidation products.

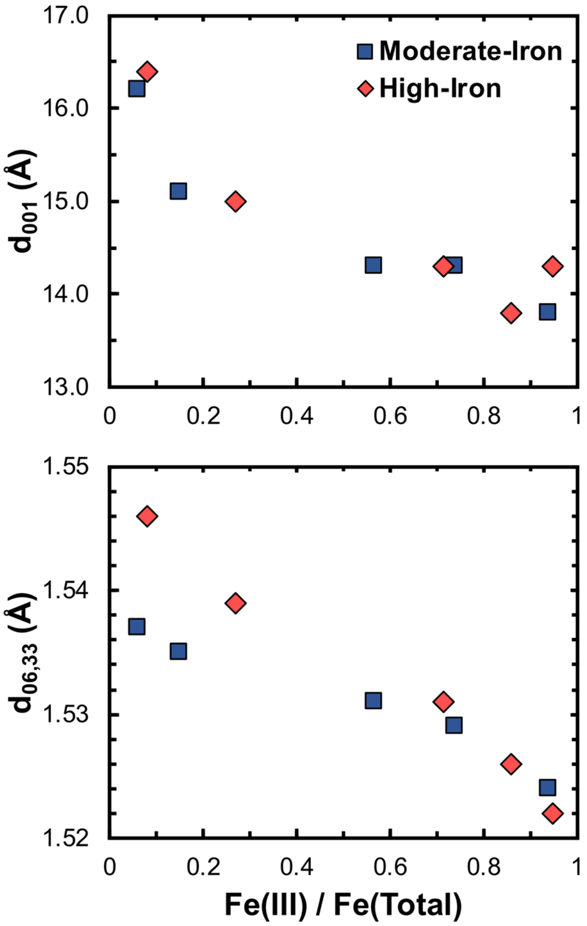

Figure 7. Relationship between the smectite (001) and (06,33) diffraction features and the extent of iron oxidation.

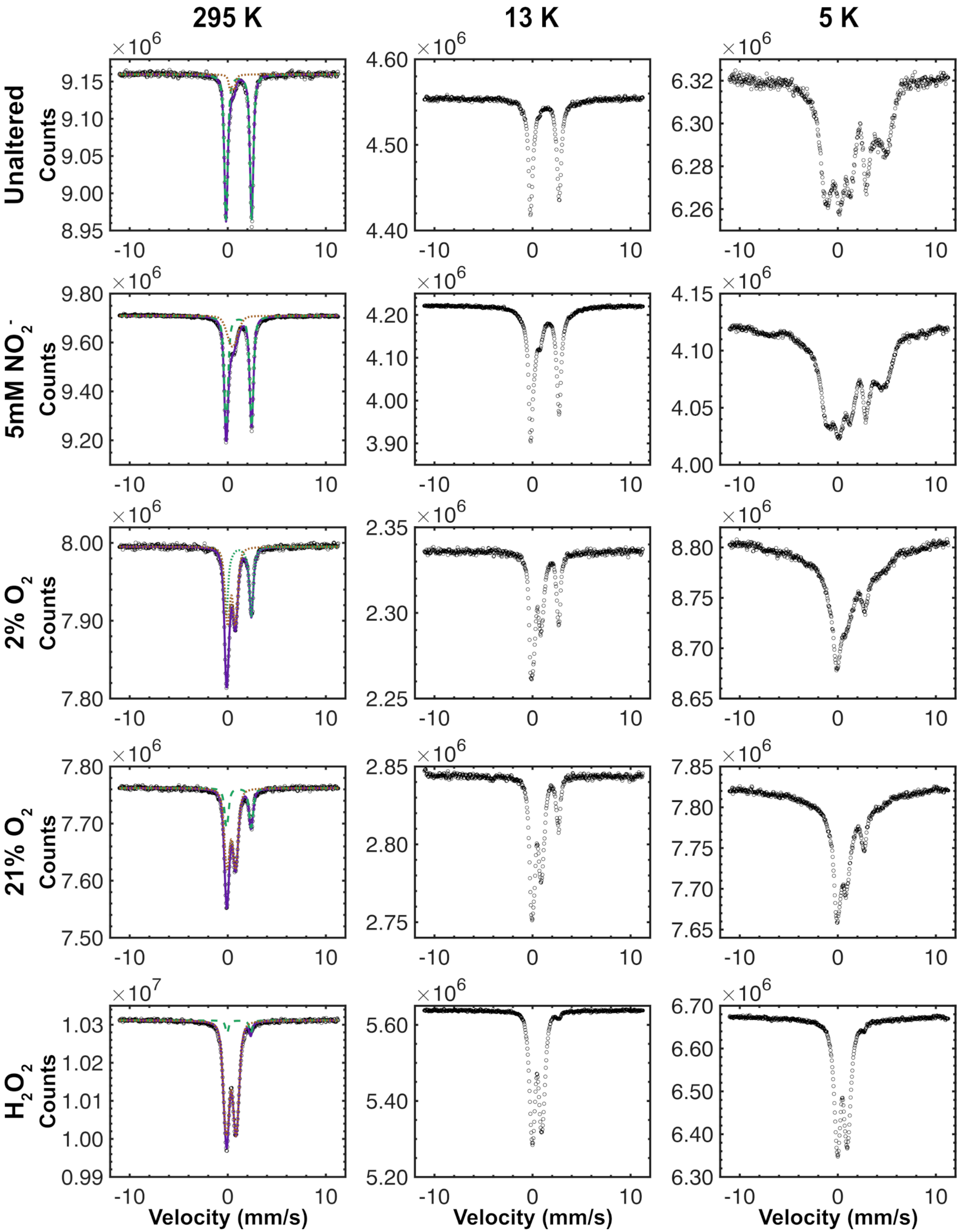

Figure 8. ^{57}Fe Mössbauer spectra of moderate-iron samples from the study, collected at 295 K, 13 K, and 5 K. Fits to the 295 K spectra in purple are the sum of ferrous and ferric components represented by dashed green and dotted brown lines, respectively.

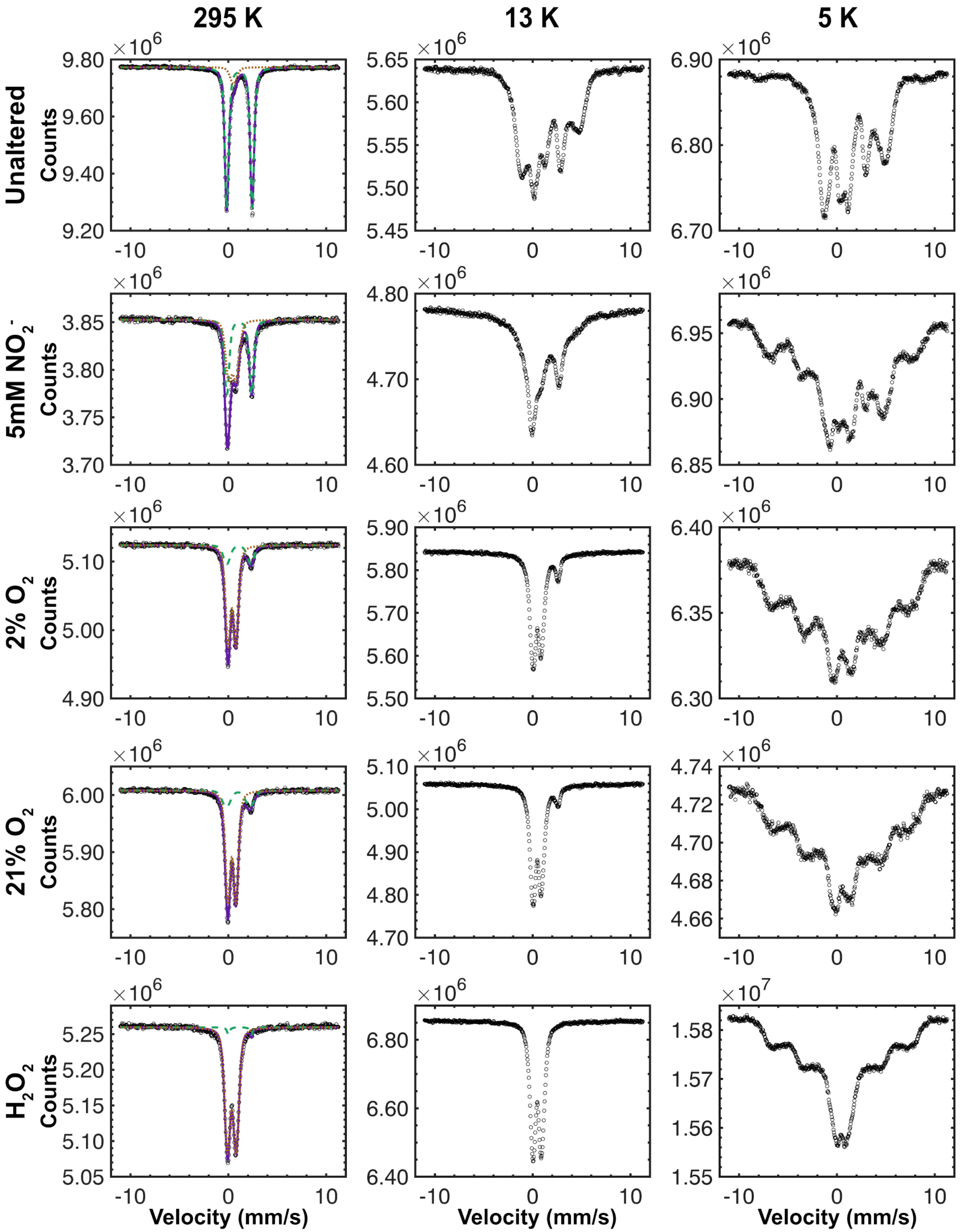

Figure 9. ^{57}Fe Mössbauer spectra of high-iron samples from the study, collected at 295 K, 13 K, and 5 K. Fits to the 295 K spectra in purple are the sum of ferrous and ferric components represented by dashed green and dotted brown lines, respectively.

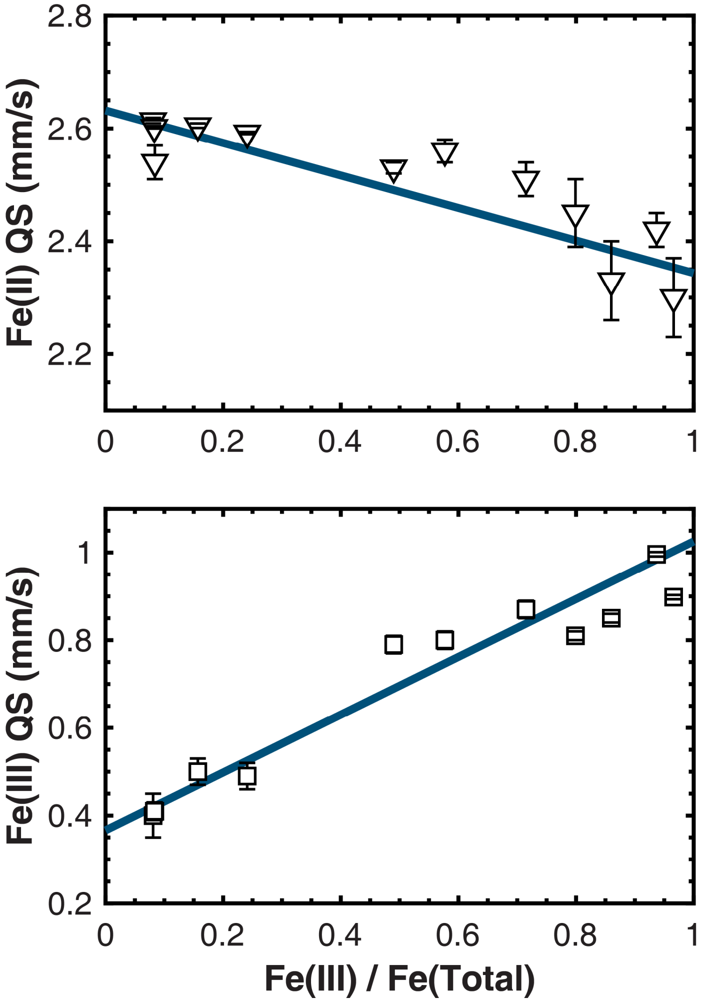

Figure 10. The relationship between the quadrupole shift (QS) of the Fe(II) and Fe(III) doublets in the 295 K ^{57}Fe Mössbauer spectra and the fraction of iron occurring as Fe(III). The lines represent linear regressions weighted by the uncertainties in the QS values.

Supplementary Material for

Rates and Products of Oxidation of Ferrous Iron in Trioctahedral Smectites

Robert J. Kupper[1], Nanqing Zhou[2], Clara S. Chan[3], Aaron Thompson[4], Jeffrey G. Catalano[1,5*]

1. Department of Earth and Planetary Sciences, Washington University, Saint Louis, MO 63130, USA

2. School of Marine Science and Policy, University of Delaware, Newark, DE 19716, USA

3. Department of Earth Sciences, University of Delaware, Newark, DE 19716, USA

4. Department of Crop and Soil Science, University of Georgia, Athens, GA 30602, USA

5. McDonnell Center for the Space Sciences, Washington University, Saint Louis, MO 63130, USA

*Corresponding author: catalano@wustl.edu

Table S1. Media composition.

Component	Concentration (mol L^{-1})
Sodium Bicarbonate	2.000×10^{-2}
Ammonium Chloride	1.870×10^{-2}
Calcium Chloride	1.794×10^{-3}
Magnesium Sulfate	4.179×10^{-4}
Dipotassium Hydrogen Phosphate	2.871×10^{-4}
Sodium Chloride	8.556×10^{-5}
Monopotassium Dihydrogen Phosphate	6.613×10^{-6}
Manganese Sulfate	2.958×10^{-6}
EDTA	1.711×10^{-6}
Iron(II) Sulfate	3.597×10^{-7}
Zinc Sulfate	3.477×10^{-7}
Cobalt(II) Nitrate	3.436×10^{-7}
Boric Acid	1.617×10^{-7}
Nickel(II) Chloride	8.414×10^{-8}
Pyridoxine Hydrochloride	4.863×10^{-8}
Sodium Molybdate	4.133×10^{-8}
Nicotinic Acid	4.061×10^{-8}
Copper Sulfate	4.005×10^{-8}
Potassium Aluminum Sulfate	3.873×10^{-8}
Disodium Tungstate	3.032×10^{-8}
Thioctic acid	2.424×10^{-8}
Thiamine	1.884×10^{-8}
p-Aminobenzoic Acid	1.588×10^{-8}
Riboflavin	1.328×10^{-8}
Calcium Pantothenate	1.049×10^{-8}
Biotin	8.186×10^{-9}
Disodium Selenite	5.782×10^{-9}
Folic Acid	4.531×10^{-9}
Vitamin B12	3.689×10^{-9}

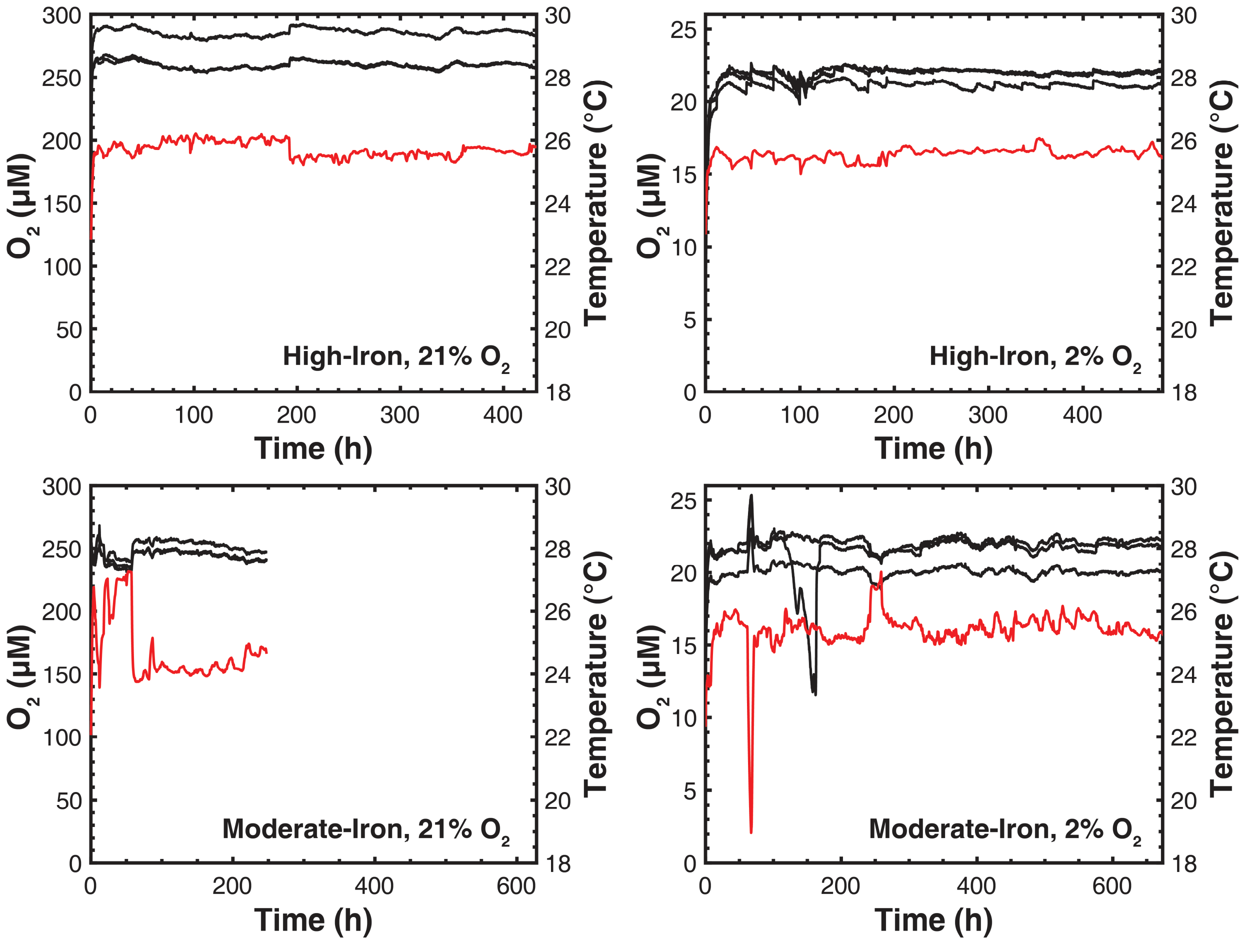

Figure S1. Dissolved oxygen and temperature measurements for the oxygen-equilibrated experiments. The black lines represent the measured oxygen concentration in each of the triplicate reactors. The singular temperature measurement is in red. A computer malfunction terminated data collection early after 250 h for the moderate-iron, 21% O_2 study. Note that the moderate-iron, 2% O_2 experiment experienced two deviations that did not perceptibly affects the results of the study. First, a building heating problem occurred between 62 and 72 h into the experiment, which appears as a transient 6°C decrease in temperature and a correspond slight increase in dissolve O_2 concentration. Second, the gas line to one reactor developed a clog at ~120 h that was corrected 40 h later, with a partial drawdown in dissolved O_2 concentration in the intervening time. This reactor showed no detectable difference in the extent of Fe(II) oxidation compared to the other two reactors after this event.

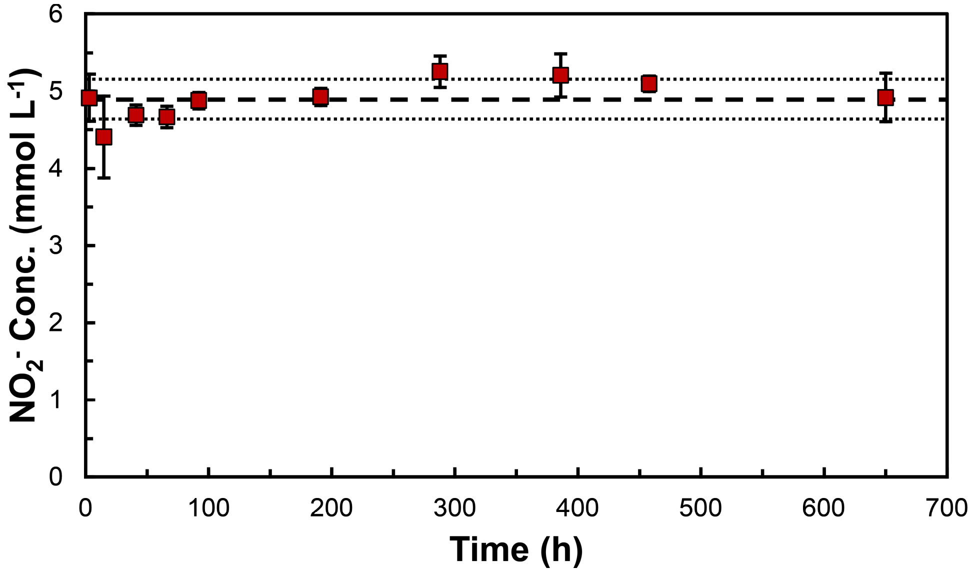

Figure S2. Dissolved nitrite concentrations during reaction with the moderate-iron smectite, reported as the mean and standard deviation of analyses of the triplicate reactors. The dashed lines show the average nitrite concentration over the course of the experiment as well as plus or minus one standard deviation of the nitrite concentration.

Section S1: Rate Equation for the Fitting of Control and Nitrite Exposed Smectites

The single site, pseudo-first order model used to fit the control and nitrite exposed smectite datasets follows a rate defined by equation A.1:

$$\frac{d[Fe(II)]}{dt} = ka_1 \tag{A.1}$$

Where k is the rate constant, and a_1 is the portion of Fe(II) governed by that rate. The integrated rate equation (Equation A.2) additionally incorporates a nonreactive portion, a_2:

$$Fe(II)_t = a_1 e^{-kt} + a_2 \tag{A.2}$$

The integrated rate equation was fit to each dataset in MATLAB using a Levenberg-Marquardt nonlinear least squares regression with each datapoint weighted by the experimental uncertainty in that point.

Table S2. Fitting parameters for the oxidant free control and nitrite exposed samples.

Smectite	**Oxidant**	**k (h^{-1})**[a]	**a_1**	**Nonreactive Fe(II) Fraction (a_2)**	**Reduced χ^2**
Moderate-Iron					
	None	0.00±0.02[a]	0±100	1±100	1.008
	NO_2^-	0.003±0.006	0.07±0.05	0.82±0.06	4.001
High-Iron					
	None	0.0±0.4	0.00±0.03	0.91±0.02	0.509
	NO_2^-	0.0009±0.0008	0.1±0.2	0.7±0.1	0.268

[a] k is the rate constant fit to the pseudo-first order kinetics and a_1 is the portion of ferrous iron controlled by that rate. The recalictrant portion is the portion determined by the model to be non-reactive.

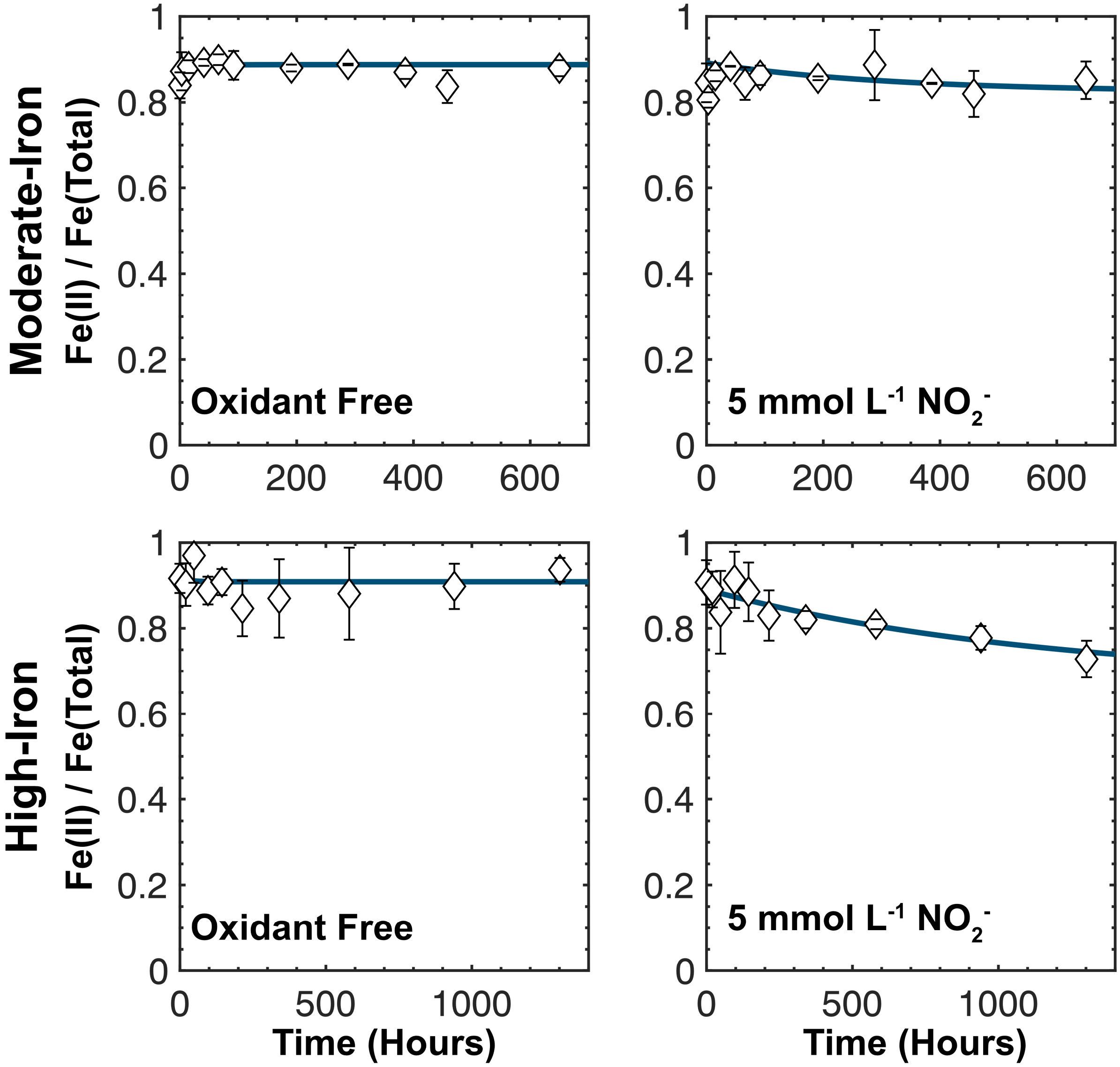

Figure S3. Fe(II)/Fe(Total) and modeled rates of oxidation for both smectite compositions (rows) for both oxidant-free controls (left) and 5 mmol L^{-1} NO_2^- (right). Open diamonds are the datapoints, with errors on each point. Solid lines are the pseudo-first order fit.

Section S2: Determination of edge sites for a hexagonal saponite particle.

An estimate of the percentage of total sites present as edge sites for a hexagonal saponite particle of a given size was obtained by modeling an ideal hexagonal brucite sheet in the Crystalmaker software. First, the smallest possible hexagonal brucite sheet of 7 magnesium sites was constructed, with six of them being edge sites and a calculated total diagonal length of 9.8 Å. From this starting point, the number of edge sites was increased incrementally by 6, one on each edge of the hexagonal sheet. With each addition, the number of non-edge sites became equal to the prior total number of sites and the diagonal length increasing by 6.2 Å. This process was used to estimate the portion os octahedral sites occurring on sheet edges as a function of clay platelet diameter (**Fig. S4**).

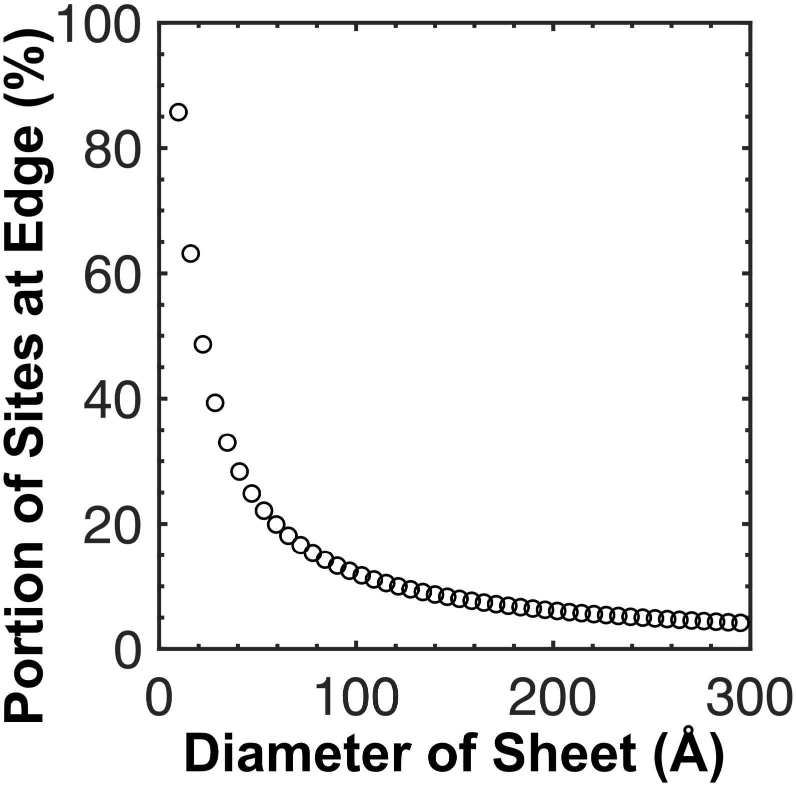

Figure S4. The percentage of octahedral sites in a simulated hexagonal brucite sheet that are present as edge sites as a function of the diameter of the sheet in Angstroms.